IMPROVING THE ACCURACY OF SOLAR SYSTEM SMALL BODY PERIOD DERIVATION THROUGH DE-ALIASING AND SURVEY CADENCE

By Daniel R. Kramer

A Thesis

Submitted in Partial Fulfillment

of the Requirements for the Degree of

Master of Science

in Informatics

Northern Arizona University

May 2023

Approved:

Michael Gowanlock, Ph.D., Co-Chair

David Trilling, Ph.D. Co-Chair

Andrew McNeill, Ph.D.

ABSTRACT

IMPROVING THE ACCURACY OF SOLAR SYSTEM SMALL BODY PERIOD DERIVATION THROUGH DE-ALIASING AND SURVEY CADENCE

DANIEL R. KRAMER

Currently, deriving small body rotation periods is one of the most challenging problems in small body astronomy. An added challenge is that data from ground-based surveys have to overcome the day-night cadence of the Earth, which causes aliasing. I used real data from the Zwicky Transient Facility (ZTF) and synthetic data from the Legacy Survey of Space and Time (LSST), several ways were tried to improve the match rate of derived small body periods to their physical state. The two main ways were (1) removing cadence based aliasing solutions after a survey has acquired observations and (2) finding a cadence for a survey that results in the highest match percentage, each of them comprising their own paper.

In my first paper, I used four different methods — three from the literature and a new one that we developed — were examined that remove aliases to improve the accuracy of period-finding algorithms. We investigate the effectiveness of these methods in decreasing the fraction of aliased period solutions by applying them to the ZTF and the LSST Solar System Products Database (SSPBD), a synthetic LSST small body dataset, asteroid datasets. We find that the VanderPlas method had the worst accuracy for each survey. The mask and our newly proposed window method yields the highest accuracy when averaged across both datasets. However, the Monte Carlo method had the highest accuracy for the ZTF dataset, while for SSPDB, it had lower accuracy than the baseline where none of these methods are applied. Where possible, detailed de-aliasing studies should be carried out for every survey with a unique cadence.

In my second paper, I used simulations of LSST to determine the best cadence for deriving small body rotation periods. LSST has already made simulations of LSST observations

using different cadences to try to determine which one is the best for many different science cases. However, these science cases do not address the derivation of small body rotation periods. We implanted synthetic asteroids in 141 different simulations, all 139 version `v2.1` simulations and two from the version `v1.7`/`v1.7.1` simulations, to determine the best and worst cadences for rotation period derivation. We found that cadences with long exposures (small errors) and cadences that repeatedly observe one field had the best derived period match rate. Conversely, short exposures and non-repeated fields had the worst match rate. We also examined the match rate as a function of survey length to examine when periods would be successfully derived. We found, with a minimum observation cut, that at least 90% of the year ten match rate is achieved in year 1. We also found that the match rate does not plateau, meaning that a longer survey would result in higher match rates.

My work in this thesis leads to several lines of future investigation: (1) Develop methods for removing pseudo-aliases, (2) Develop a "confidence" metric for period solutions, (3) testing the de-aliasing methods and the effects of cadence on period derivation on stellar and non-sinusoidal sources, and (4) analyzing the difference between the real LSST period results and the synthetic.

ACKNOWLEDGMENTS

Thank you to my parents, Steven and Betsy Kramer, for enabling me in my education.

Thank you to everyone in the Trilling Research Group, especially Colin Chandler, Annika Gustafsson, Andy Lopez-Oquendo, Ryder Strauss, and Maria Chernyavskaya.

Thank you to everyone in the Gowanlock Research Group, especially Benoit Gallet, Brian Donnelly, Kaitlyn Lee, and Felicity Escarzaga.

Thank you to Cmdr. Raymond Schenk and Jordan Smith for helping me discover a love for computer science and physics during my time at Johns Creek High School.

Table of Contents

List of Tables

List of Figures

Acronyms

Below are the acronyms used and the page number where they first appear.

Chapter 1

Introduction

Period finding has been one of the most important areas of research in modern times, with period finding algorithms like the Fast Fourier Transform [14] being called "The most important numerical algorithm of our lifetime" [60] and the Quantum Fourier Transform [16] leading the way for many quantum computer algorithms. Solar System small body science is no stranger to period finding, with more than 40,000 objects having a known rotation period [62, 67]. However, there are currently 1.2×10^6 [45] known small bodies, so there is a major gap between known objects and objects with known rotation periods. This problem is about to become more acute in the coming years with new, large scale surveys starting (Section 1.2.1.1). The rotation period for a Solar System small body is an important property, allowing us to determine the origin and evolution [11, 12, 56] and physical properties [44] of the object. However, deriving small body rotation periods is not straightforward, the cadences of ground based, large scale surveys do not allow for periods to be easily determined for all objects (Section 1.2.2.1).

Modern large scale surveys introduce a new problem in astronomy that past astronomers have not had to deal with, a vast amount of data (big data) in which no human could manually analyze. This problem requires a new profession in both astronomy, computer science, and data analysis: astroinformatics. Astroinformatics is a new field for large scale data analysis for astronomy. Astroinformaticists use High Performance Computers and advanced algorithms to find answers in astronomy in large scale survey data.

Period finding is a computing challenge. One of the most widely used and simplistic period finding algorithms for astronomy, Lomb-Scargle (L-S, Lomb [38], Scargle [57]), has a time complexity, a measure of about how long an algorithm takes to compute, of $O(nm)$, where n is the number of observations for an object and m is the number of frequencies (more detail on L-S and its time complexity is presented in Section 2.2.1). Usually, n is around 50-1000 and m is $> 1 \times 10^5$, meaning that millions of computations are needed to determine a period for an object. With large scale surveys observing hundreds of thousands or millions of objects, astroinformatics is needed to compute the periods.

1.1 The Solar System

The Solar System is the region of space where the Sun's gravity dominates. It is made up of the Sun, planets, satellites/moons, and small bodies[1]. Figure 1.1 shows the location of objects in the Solar System. The small bodies (blue dots) are located all throughout the Solar System.

Most of the known small bodies are in the following six groups, in order of distance from the Sun:

1. *Near Earth Objects/Asteroids* — Objects that have a perihelion distance of less than 1.3 AU.

2. *Asteroid/Main Belt* — Objects between the orbit of Mars and Jupiter and have a semi-major axis between 2.2 AU to 3.2 AU.

3. *Hildas* — Objects in a 3:2 orbital resonance with Jupiter.

4. *Jupiter Trojans* — Objects at Jupter's L_4 and L_5 points, orbiting in a 1:1 resonance.

5. *Centaurs* — Objects within the orbits of the Gas and Ice Giants.

6. *Trans-Neptunian Objects (TNOs)/Kuiper Belt* — Objects beyond the orbit of Neptune.

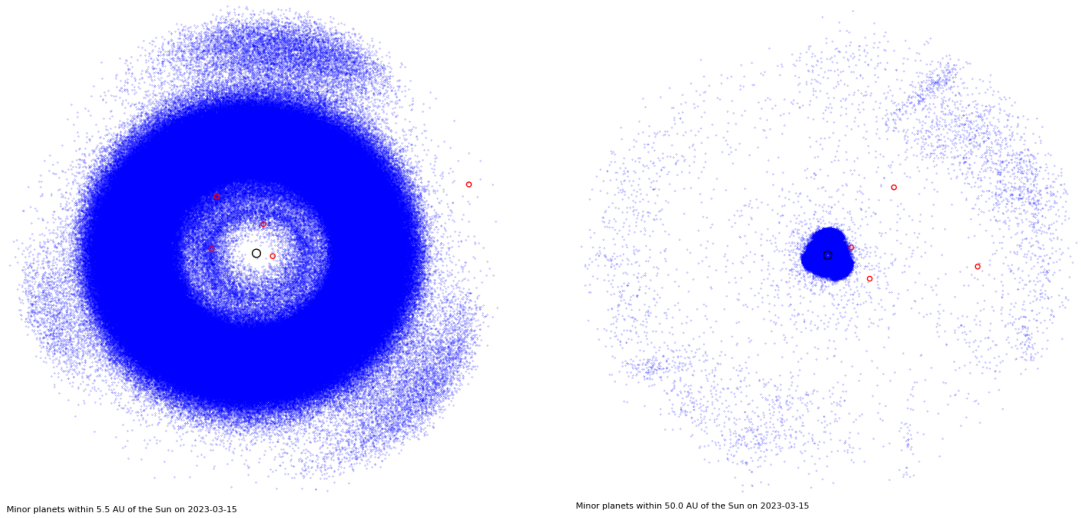

(a) Inner Solar System (b) Outer Solar System

Figure 1.1: Source: Minor Planet Center [45]. The known objects in the Solar System on 2023-03-15. The black circle is the Sun, the red circles are the planets and the blue dots are small bodies.

Most of the known small bodies are in the Asteroid Belt (which is why "small bodies" are sometimes called "asteroids"), but this is caused by observation bias as the asteroids are "close" to Earth and "large". Most small bodies are TNOs [43], but they are far from the Earth/Sun, and therefore, too dim to observe. However, TNOs are larger by a factor of 1000, on average, compared to the asteroids [35].

1.2 Surveys

The main way small bodies are discovered/observed currently are through astronomical surveys, an observing strategy to observe a general region of the sky, not a specific object. Most surveys are not targeting on small bodies, but because small bodies are the closest objects to the Earth[2], they will always be inadvertently observed[3], making surveys excellent sources of small body data.

[1]Dwarf Planets, like Ceres and Pluto, are counted as small bodies.
[2]Not including the other bodies in the Solar System.
[3]Assuming the survey is observing in wavelengths small bodies reflect/emit.

1.2.1 All Sky Surveys

All Sky Surveys are a type of survey that observes the entire sky. There have been many examples of these kind of surveys [18, 22, 42, 54, 59], but this section will focus on Zwicky Transient Facility (ZTF, Bellm et al. [10]) and Legacy Survey of Space and Time (LSST, Ivezić et al. [32]) as they are the two surveys used throughout this thesis.

1.2.1.1 Legacy Survey of Space and Time

The Vera C. Rubin observatory is a new, all sky survey being built in Chile which will house the LSST. It will produce about 500-1000 observations for about 40 billion sources. About 5 million of these objects will be small bodies. Therefore, the number of known small bodies will grow by about five times.

LSST is scheduled to start in 2024[4] and run for 10 years. To prepare for science operations, synthetic LSST data has been created, since, at the time of writing, LSST has not started observing. There are two sources to obtain synthetic small body LSST data: LSST Solar System Product Database (SSPDB, Juric et al. [34]) and generating from LSST simulations [34]. Chapter 2 used SSPDB data while Chapter 3 used the simulations.

1.2.1.2 Zwicky Transient Facility

ZTF is an all sky survey from the Palomar observatory located in California, USA that has been operating since 2018. It is acting as a LSST precursor, operating at about one-tenth LSST scale. As of this writing, ZTF has $> 21 \times 10^6$ small body observations, but only a subset of the observations was used, SNAPShot1 [62], because of a period of erroneous observations from ZTF. SNAPShot1 used observations from 2018–07–19 to 2020–05–19, using only numbered asteroids with more than 50 observations with Real-Bogus scores ≥ 0.55 [19].

[4] `https://docushare.lsst.org/docushare/dsweb/Get/Document-35216`

1.2.2 Targeted Surveys

The other type of surveys are targeted surveys, like the Transiting Exoplanet Survey Satellite (TESS, Ricker et al. [54]) and DECam Ecliptic Exploration Project (DEEP, Trilling [61]). These surveys only observe a small number of fields[5], but their constant observing allows for consistent data.

A complication of working with small bodies is that they move on the sky. If an object is near the edge of a field, it could move out of the field before the survey is over. Objects that move out would have a fraction of the data objects that stay in the field receive. DEEP, which is a search for TNOs, has to account for this by moving the fields slightly each year they observe. TESS, where small body observations are a byproduct, does not account for this and loses the objects.

1.2.2.1 Issues with All Sky Surveys

ZTF, LSST, and all ground based, all sky surveys[6] cannot observe during the day. This causes an inevitable, day-related signal in period deriving efforts, called aliasing. Aliasing results in a significant proportion of derived periods to be at 24 h and related times (12 h, 24 h, 48 h, and 96 h, among others). These derivation results require more human intervention and/or compute time to label or fix. As LSST will observe about 5 million small bodies, most with enough observations to derive a period[7], human intervention is not feasible and the algorithms used need to be fast and scalable.

Targeted surveys, however do not face this challenge as their consistent observations suppress the aliasing, For example, DEEP, which is a ground based survey, avoids aliases by only running for a few days a year along with having consistent observations of only six fields; the day-related signals do not "have time" to appear and they are drowned out by

[5]TESS is technically an all sky survey, but it observes a single field for up to 27 days, so it can also count as targeted

[6]That do not observe in radio.

[7]50 observations is the cutoff used for the work presented here.

the real period. TESS is space based, so it naturally does not have day-related aliases.

Chapter 2 aims to remove aliases after observations have been recorded and Chapter 3 aims to aid LSST and future surveys in picking cadences that increase the overall number of accurate period results.

1.3 Other Publications

Bellow are other publications I have been a part of but not led, in order of publication:

1. *Erasmus et al. [20]* — Asteroid Terrestrial-impact Last Alert System (ATLAS, Denneau [18]) and ZTF photometry was used to discover the slowest known rotating small bodies. The previous slowest rotating small body was (2056) Nancy with a period of 1343 h. We found 32 with longer periods, the longest being 52534 with a period of 4812 h.

2. *Gowanlock et al. [24]* — We implemented L-S on a GPU. More information about L-S in Section 2.2.1.

3. *Trilling et al. [62]* — This was the release of SNAPShot1, a dataset of 31,693 small body physical properties from ZTF observations. This dataset also contained rotation periods for these objects.

1.4 Organization

This thesis is organized as follows: Chapter 2 is my first first author, *Removing Aliases in Time-Series Photometry* (Kramer et al. 36), which goes over de-aliasing after a survey has observed, Chapter 3, which is my second seconds paper, *The Effect of Different LSST Cadences on Derived Rotation Periods for Solar System Small Bodies* (submitted, Kramer et al. 37), which determines the best LSST cadence for deriving asteroid rotation periods, and Chapter 4, goes over my overall conclusions. Appendix A contains the appendices for

Chapter 2, Appendix B has a guide on how to perform period derivation for an object, and Appendix C contains information about phase curves and how to derive an object's absolute magnitude and slope parameter.

Chapter 2

Removing Aliases in Time-Series Photometry

Daniel Kramer[12], Michael Gowanlock[12], David Trilling[21], Andrew McNeill[23], Nicolas Erasmus[4]

Accepted to Astronomy and Computing *on 2023-04-24.*

2.1 Introduction

Determining periodic behavior among astrophysical sources is useful for describing their physical properties. For example, the internal strength of an asteroid can be determined using, among other observed properties, its rotation period [44]. Light curves have also been used to categorize a star's stellar type [8].

Ground-based telescopic surveys that produce sparse data inevitably have signals in the object's periodogram— typically at or near 12 h, 24 h, 48 h, and 96 h — related to the day-night cycle of the Earth. These cadences cause aliasing, an effect where there are peaks in a periodogram that are not at the real period of an observed object.

If the output of a period-finding method and its corresponding light curve is visually examined, an astronomer can potentially make a judgment if a derived period is an alias

[1]School of Informatics, Computing, and Cyber Systems, Northern Arizona University, Flagstaff, AZ 86011, USA
[2]Department of Astronomy and Planetary Science, Northern Arizona University, Flagstaff, AZ 86011, USA
[3]Department of Physics, Lehigh University, 16 Memorial Drive East, Bethlehem, PA 18015, USA
[4]South African Astronomical Observatory, Cape Town, 7925, South Africa

or not. With large-scale surveys, like the Legacy Survey of Space and Time (LSST, Ivezić et al. [32]), too many objects will be observed for humans to manually confirm each derived period. This requires automating both deriving the periods and determining if the period is correct.

The problem of period-finding at scale will become more acute when LSST is producing data, as more than 100 million periodic sources are expected in the LSST catalog [39]. If, for example, 20% of period solutions are aliases, then 20 million sources would have incorrectly derived periods. The incorrect periods would either (1) be naively included in a catalog, (2) have solutions at common alias periods discarded, or (3) have to be examined with some verification algorithm. Any method that reduces the total number of alias results improves the three outcomes by (1) reducing the number of bad solutions, improving the overall accuracy, (2) increasing the overall number of correct solutions, or (3) decreasing the amount of computation to verify/score the periods.

While this is an important problem for ongoing and upcoming surveys, there has been little progress on de-aliasing methods for sparse data. For instance, Carbonell et al. [15] has examined the de-aliasing properties of past methods, notably CLEAN [55]. However, those methods only work on time series data with uniform observations during the night. Since modern ground-based surveys generate sparse data that is not uniform, these methods are unsuitable for these surveys. Recently, several papers have used some de-aliasing techniques using large scale survey data [17, 20, 29], but none tested the improvement their method had over no de-aliasing.

In this paper, we analyze the performance of four approaches to de-aliasing, with performance and period-finding accuracy in mind.

The paper is organized as follows: Section 2.2 discusses the Lomb-Scargle periodogram, Section 2.3 gives an overview of the datasets used, Section 3.2 gives an overview of the four methods that were tested, Section 3.3 discusses the results of the four methods, Section 3.4 provides our discussion of the results of the paper, and Section 3.5 presents our conclusions

and some future work on this and related problems.

2.2 Period Finding Algorithms

For testing the accuracy of the different de-aliasing methods, a period finding algorithm is needed. In this section, we will discuss four different methods, Lomb-Scargle (L-S, Lomb [38], Scargle [57]), SuperSmoother [21], Conditional Entropy [25], and Bootstrap χ^2 [64], and why L-S is used as the method for this analysis.

2.2.1 Lomb-Scargle

L-S is a period-finding method first developed by Lomb [38] and later improved by Scargle [57]. It is one of the most popular period-finding algorithms used in astronomy. The general approach is to calculate the periodogram power, essentially a measure of the goodness of the solution, through Equation 2.1 as follows.

$$\begin{aligned} P(f) &= \frac{1}{2}\left\{ \frac{\left(\sum_n g_n \cos(2\pi f[t_n-\tau])\right)^2}{\sum_n \cos^2(2\pi f[t_n-\tau])} \frac{\left(\sum_n g_n \sin(2\pi f[t_n-\tau])\right)^2}{\sum_n \sin^2(2\pi f[t_n-\tau])} \right\} \\ \tau &= \frac{1}{4\pi f}\tan^{-1}\left(\frac{\sum_n \sin(4\pi f t_n)}{\sum_n \cos(4\pi f t_n)}\right) \end{aligned} \tag{2.1}$$

Here, $P(f)$ is the power for an angular frequency f, g_n is the observed telescopic magnitude of observation n and t_n is the time of observation n. Higher powers indicate a greater likelihood that f is the angular frequency of the observed object. Note that the Lomb-Scargle Periodogram (LSP, Lomb [38], Scargle [57]) has a time complexity of $O(nm)$, where n is the number of observations used and m is the number of frequencies examined.

A periodogram is typically computed by calculating powers for a range of frequencies (or periods) in $[f_{\min}, f_{\max}]$ that are sampled over a uniform frequency space. Ideally, there would only be a peak in the periodogram at the angular frequency f that corresponds to

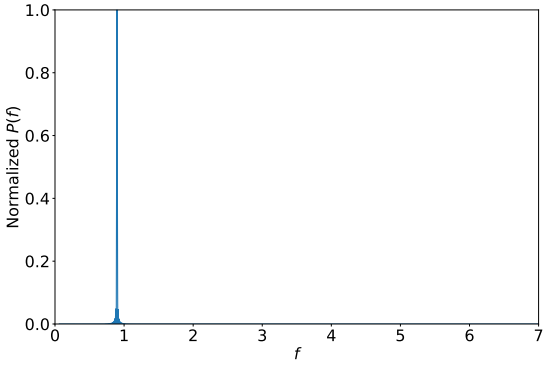

(a) Uniformly sampled sine wave.

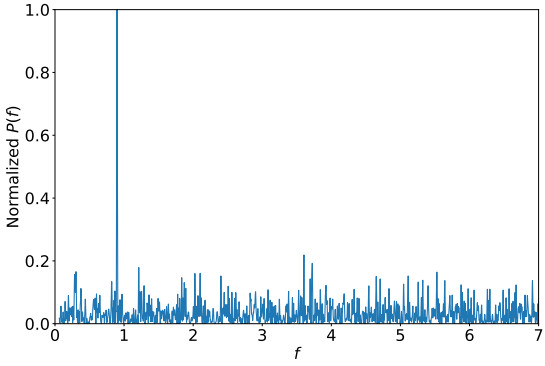

(b) Randomly sampled sine wave.

Figure 2.1: The periodograms for a uniformly sampled sine wave and a random sample of it. The x-axis is the angular frequency and the y-axis is the normalized power. The sine wave was given an angular frequency of $2\pi/7$ (period of 7) and an amplitude of 0.3. The pure sine wave used 1000 points and the sampled sine wave used 0.5% of those points, for about 50 total points used.

the object's physical rotation state, with all other values of $P(f)$ having a value of zero. In reality, because of uncertainties in the measurements, a non-uniform cadence, and aliasing, the periodogram is often noisy with multiple peaks, so determining the correct peak is not always straightforward. Figure 2.1 shows how a periodogram generated with a uniformly sampled sine wave with a small Δt compares to a randomly sampled sine wave's periodogram. The randomly sampled sine wave's periodogram is noisy around $P(f) = 0$ while the uniformly sampled sine wave only has a peak at the sine curve's frequency.

2.2.2 Other Algorithms

Other period finding algorithms exist, like SuperSmoother [21], Conditional Entropy [25], Bootstrap χ^2 [64], among others. With all of these algorithms, there is a trade-off between accuracy, speed, space, and light-curve shape flexibility. We summarize the three algorithms above as follows:

- *SuperSmoother* is especially useful for periodic signals that are not sinusoidal [9, 30], has a time complexity and space complexity of $O(nm)$, and it is susceptible to aliasing [23].

- *Conditional Entropy* also has time complexity of $O(nm)$, is less accurate than L-S for fast periods, and is susceptible to aliasing [17].

- *Bootstrap* χ^2 is the slowest, with a time complexity of $O(snm)$, where s is the number of bootstrap samples, but it is the most accurate, with aliasing having the smallest effect on this method compared to the others described above [64].

L-S has the same time complexity as SuperSmoother and Conditional Entropy, all three being smaller than Bootstrap χ^2. As SuperSmoother has a space complexity of $O(nm)$ while L-S and Conditional Entropy have a space complexity of $O(n+m) \approx O(m)$, SuperSmoother was not used. Finally, since L-S and Conditional Entropy are similar, and L-S is the the standard algorithm used for deriving the periods in astronomy, we elect to use L-S in this paper. However, any period finding algorithm that produces a periodogram is capable of implementing the methods described in Section 3.2.

2.3 Data Used

The upcoming LSST— to be carried out with the Vera C. Rubin Observatory that is presently under construction in Chile — will revolutionize many fields of astronomy [32]. LSST will generate sparse photometry on the around 500–1000 measurements over ten years

for some 40 billion astronomical sources. The vast majority of these will be sidereal objects (stationary on the sky); around 5 million of them will be moving objects. Many of these LSST-observed sources will be variable, with regular periods, so it is of interest to develop and implement accurate period-finding algorithms that can operate at the vast LSST scale.

The ongoing all-sky survey being carried out by the Zwicky Transient Facility (ZTF, Bellm et al. [10]) acts as a kind of LSST precursor. ZTF is carrying out a public survey that is very LSST-like in terms of cadence, data type, and data accessibility, but at something like one-tenth the LSST scale.

The work presented here has its origin in Solar System science and asteroid period finding but is relevant for period-searching for any kind of astrophysical source in either ZTF or LSST data. For ZTF, we used asteroid data from SNAPShot1 [62], which used ZTF observations from 2018–07–19 to 2020–05–19, using only numbered asteroids with more than 50 observations with Real-Bogus scores ≥ 0.55 [19]; the Real-Bogus cut eliminated about 9% of all observations.

There is no actual LSST data yet as science operations will commence in 2024, so we used the LSST Solar System Product Database (SSPDB, Juric et al. [34]), a complete simulation of asteroid observations over the 10 year nominal lifetime of LSST, as our LSST testbed. However, the objects in this synthetic database are all assumed to be spherical and thus, unlike almost all real asteroids, do not show shape-induced periodic variability in the lightcurves. We therefore assigned lightcurve amplitudes and rotation periods to each SSPDB object, as described in Appendix A.1.

2.4 Methods

In this section, we present our de-aliasing analysis on the ZTF and SSPDB asteroid data sets. We use three methods from the literature — masking; Monte Carlo (MC); and VanderPlas (VP)— and present our new approach, the window method. Broadly speaking, the MC method tries to remove aliasing through subsampling (with multiple trials), whereas

the other methods attempt to remove signals at the expected alias periods.

One method that will not be tested is the False Alarm Probability [7]. False Alarm Probability is sometimes incorrectly used as a proxy for the goodness of a L-S solution. However, False Alarm Probability is a way of calculating the probability $p = (\text{power}|\text{noise})$: the probability that a given periodogram power is part of the noise of the periodogram [7, 63]. If there is an alias peak with a larger $P(f)$ than the real peak, then it would have a lower False Alarm Probability. Because False Alarm Probability is not testing for the authenticity of a signal related to the physical period in the system being monitored, it is not a useful method for determining if a peak is a real period or an alias.

2.4.1 Masking

Masking is the most straightforward approach presented in this paper: solutions near the known alias solutions are simply rejected. The alias periods or a small range around the alias can be removed (masked out) from the periodogram so the real period's peak would therefore have the largest remaining $P(f)$. Usually, there are multiple aliases, so several masks are needed to remove them.

This method was used in Erasmus et al. [20], which presented asteroid photometry from Asteroid Terrestrial-impact Last Alert System and ZTF where they masked out periods of {8, 12, 16, 24, 48} hours. The remaining periodogram peaks with the largest power were then found to be those representing super-slow rotation periods. Erasmus et al. [20] showed that the masking method is a viable way of removing alias period solutions so we incorporate this method into our analysis. This method was also used in Coughlin et al. [17], which used a similar method to derive the mask ranges as described below. The Coughlin et al. [17] mask ranges, in rotation period space, are [(0.5, 0.5), (0.51, 0.51), (0.52, 0.52), (5.93, 6.08), (7.87, 8.14), (11.71, 12.31), (22.86, 25.26), (46.15, 50.0), (600.0, 800.0)] hours.

Table 2.1 and Figure 2.2 show the period ranges that are masked out for each dataset. The mask ranges were derived through the following steps:

Dataset	Mask Ranges
ZTF	(4.789, 4.814), (5.989, 6.014), (7.972, 8.014), (11.947, 12.039), (23.764, 24.164)
SSPDB	(4.789, 4.839), (5.939, 6.039), (7.939, 8.039), (11.889, 12.039), (23.639, 24.239)

Table 2.1: The period ranges (exclusive) for each of the datasets to be excluded from the (light-curve) period space. Note that these ranges are light curve periods, not rotation periods, where an object's light curve period is half its rotation period.

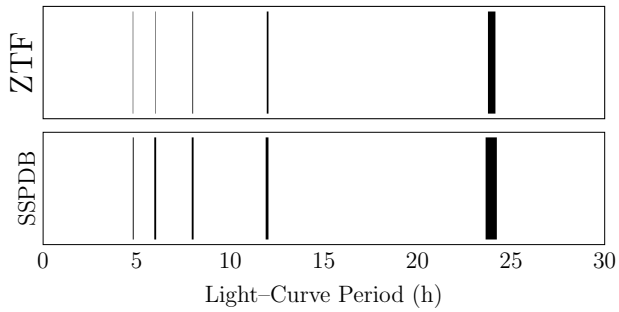

Figure 2.2: Visualization of the mask ranges from Table 2.1. The black bars indicate the masked regions where all solutions are rejected. ZTF and SSPDB have similar, but not exactly the same, ranges.

1. Generate a histogram of the derived periods.

2. Create a new mask range by selecting the bin with the highest number of objects. For example, if the bin with the most objects is $[23.9\,\mathrm{h}, 24.1\,\mathrm{h}]$, then it would be added as a mask range.

3. Re-derive the periods with this new mask range.

4. Repeat steps 1 through 3 consecutively, adding new masks. Then select the mask ranges that provide the maximum match percentage to a database of accurate periods for the objects. For example, Figure 2.3 shows percent match against the Light Curve Database (LCDB; Warner et al. 67) as a function of the number of masks for ZTF.

The ranges for both ZTF and SSPDB are similar (Table 2.1 and Figure 2.2), but not all surveys will have these same ranges because they will have different cadences and different observational errors. Despite this, we expect that all ground-based surveys will have the 24 h

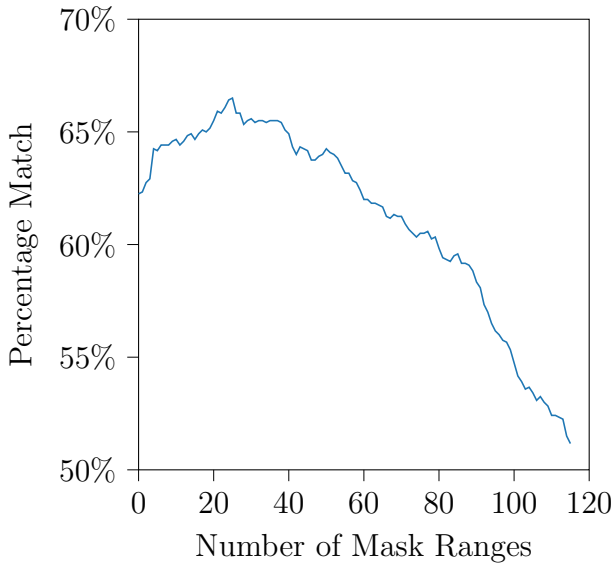

Figure 2.3: The match percentage for each new mask range. The x-axis is the number of 0.05 h size mask ranges. The y-axis is the match percentage.

Year	1	2	3	4	5	6	7	8	9	10
24 h Mask Width (h)	0.44	0.75	0.68	0.63	0.58	0.60	0.60	0.83	0.60	0.60

Table 2.2: The widths of the mask around 24 h for SSPDB observations up to Year 1, 2, 3, etc.

alias. Even though ZTF and SSPDB are similar surveys, SSPDB's mask ranges are "wider" than ZTF's. The reason for this is probably because of slight differences between the two surveys and SSPDB's longer timescale. Table 2.2, which is the widths of the mask around 24 h for observations of SSPDB up to year 1, year 2, etc. The size of the 24 h mask range fluctuated on the range of 0.44 h to 0.83 h, which are all greater than ZTF's 24 h mask range size of 0.40 h. The widths do seem to converge on a width of 0.60 h but Year 8's mask width does not follow the trend.

Advantage: The primary advantage of this approach is that it is the fastest to compute. The time complexity for the method is $O(nm)$, where n is the number of data points used and m is the number of frequencies examined. If the masks are pre-computed, the run time is slightly faster compared to a normal LSP because, with the same frequency range and Δf, fewer frequencies (m) would have to be examined as the frequencies in the mask ranges

would be excluded.

Disadvantage: This method has the disadvantage that true periods that are within one of the masked ranges will never be identified. The LCDB contains a large number of curated asteroid rotation periods and only about $1\% - 2\%$ of objects in the LCDB have rotation periods that are in the masked ranges of Table 2.1, so only a low number of objects would be impacted.

2.4.2 Monte Carlo (MC)

Since aliases are generated by the observing cadence intervals, randomly subsampling the observations, across many trials, might suppress the signal from the aliases. An overall periodogram for each asteroid can then be found either by finding the most common peak power from each trial's periodogram, or by summing over all the periodograms. Some attention must be paid to ensure that the time baseline of the subsample ($T_{\rm sub}$) is greater than $P_{\rm max}$, the period corresponding to the minimum frequency examined, otherwise, L-S will derive the period of a partial light-curve, causing an incorrect period to be derived. For large scale surveys, like ZTF and LSST, that produce sparse photometry over years, this is not an issue as $T_{\rm sub}$ will always be greater than $P_{\rm max}$ for any reasonable $P_{\rm max}$.

For the calculations in this paper, we used 100 selection samples/trials (i) per object with 50 random observations (n). SSPDB objects had to have at least 200 observations while ZTF objects only had to have 90 observations so there would be enough objects to get a large statistical sample. These parameters were found via an ad hoc process of changing the minimum number of observations required, the number of observations per subsample, and the number of MC trials to find a high match percentage.

Finally, we sum the un-normalized periodograms over all trials to yield the overall periodogram. The highest peak from this periodogram is used as the derived period.

Advantage: This method has the advantage that, compared to the other methods, it is the most oblivious to aliases like those in Table 2.1. Unlike the masking method, the MC

method could derive a correct rotation period that happens to be an alias.

Disadvantage: This method also requires more observations than the other methods discussed because in order to produce a credible periodogram, the number of observations in each subsample needs to be sufficiently large while also being significantly smaller than the total number of data points. This is needed so that pairs of observations that are, for example, 24 h apart are excluded from the same subsample.

This method is also the slowest, with a time complexity of $O(nmi)$, where n is the number of data points used for each iteration, m is the number of frequencies checked, and i is the number of selection samples.

2.4.3 Window

The window function derives aliases caused by the observational cadence. It takes the temporal data from an object's observations to produce a periodogram-like output where a frequency having a high power corresponds to high aliasing [63].

$$\mathcal{P}_w(f; \{t_n\}) = \left| \sum_{n=1}^{N} e^{-2\pi i f t_n} \right|^2 \tag{2.2}$$

Equation 2.2 shows the window function, but VanderPlas [63] showed that a LSP can be used as an approximation of the window function if in Equation 2.1, $g_n = 1$; this simulates a completely spherical, homogeneous object. Therefore, any signal present in the window periodogram would be aliasing caused by the underlying cadence.

Figure 2.4 provides an example of how an object's LSP and window periodogram relate. There are three key observations from Figure 2.4: (1) there are peaks in the LSP that do not correspond to the real period, (2) all of the significantly strong peaks that are in the window periodogram also appear in the LSP, and (3) there exist peaks in the LSP that are not the real period or in the window periodogram; these are pseudo-aliases. The example pseudo-alias marked in Figure 2.4 is $((1/P) - (1/24\,\mathrm{h}))^{-1}$ where P is the real period for the

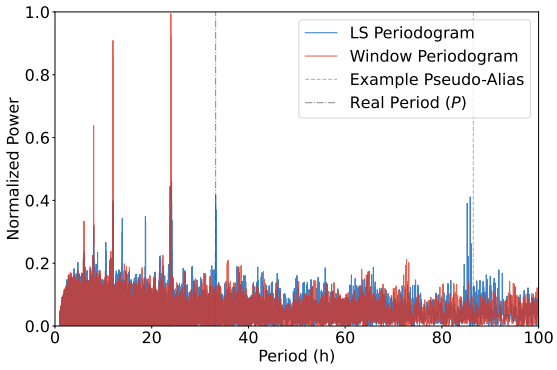

Figure 2.4: The LSP and window periodogram for an object from SSPDB. The LSP is in red and the window periodogram is in blue. The given period for the object is marked by the dash-dot-dash line and its peak is only present in the LSP. The dashed line marks an example pseudo-alias which is also only present in the LSP. The peaks in the window periodogram are the aliases which are also all present in the LSP.

object [64].

Previous algorithms that use the window function, like deconvolution and CLEAN, do not work for removing aliases [63] because they assume that the strongest peak in the periodogram is the peak that corresponds to the real period. Here we present a new way to use the window function to remove aliases, where the pseudocode can be found in Algorithm 1. This differs from deconvolution and CLEAN because they rely on deconvolution for their alias removal while Algorithm 1 does not.

Algorithm 1 takes an object's time of observation $T = \{t_1, t_2, \ldots, t_n\}$ (time), observed magnitudes $G = \{g_1, g_2, \ldots, g_n\}$ (mag) where n is the number of observations, and the frequency grid on $[f_{\min}, f_{\max}]$ (freqs) as arguments. The `LS` and `Window` functions on lines 2 and 3 calculate the L-S and window periodograms respectively. The `findPeaks` methods on lines 4 and 5 find the peaks in those periodograms and returns the peak frequencies and their powers. Line 6 sorts the LSP peaks by their power in descending order. Line 9 loops until the current LSP peak is not contained in the window peaks. If the LSP peak is in the set of window peaks, the index of the current peak is incremented. Line 12 tests if all of the detected LSP peaks have been compared against the set of window peaks. If they have,

Algorithm 1 Our method of using the peaks in the window periodogram to check if a peak in the LSP is an alias.

```
1: procedure windowMethod(time, mag, freqs)
2:     pgramLS ← LS(time, mag, freqs)
3:     pgramWindow ← Window(time, freqs)
4:     LSPeaks ← findPeaks(pgramLS)
5:     WindowPeaks ← findPeaks(pgramWindow)
6:     sort(LSPeaks)
7:     NPeaks ← length(LSPeaks)
8:     index ← 0
9:     while index < NPeaks and LSPeaks[index] ∉ WindowPeaks do
10:        index ← index+1
11:    end while
12:    if index ≥ length(LSPeaks) then
13:        correctPeak ← LSPeaks[0]
14:    else
15:        correctPeak ← LSPeak[index]
16:    end if
17:    return correctPeak
18: end procedure
```

then the peak with the highest power is used as the correct peak (although this is probably an alias), otherwise, the peak at the current index is used as the correct peak. The correct peak is then returned. A python implementation is available as a GitHub gist here[5].

Advantage: This method has a distinct advantage over the masking method. The window function exposes aliases on a per-object basis, whereas the masking method uses a single set of masks for all objects in a catalog. Consequently, the window method may enable finding correct periods that are typical aliases (e.g., those defined in Section 2.1), whereas the masking method excludes all of these periods.

Disadvantage: Using Algorithm 1, this method has the same time complexity for L-S as the other methods, which is $O(nm)$. It also has an additional time complexity for the peak finding algorithm, Ψ, which we describe below. However, since this method requires two LSP to be calculated, it is at least twice as many operations as the LSP. The implementation for the window periodogram peak finding function considered any power greater than 5σ from

[5] `https://gist.github.com/drk98/6b15633e8fc43e8daf6b628548006376`

	L-S Min. Peak Height	L-S Peak Order
ZTF	1/7	10,000
SSPDB	1/10	3000

Table 2.3: The parameters for the window/VanderPlas methods. "L-S Min. Peak Height" is the minimum power of a peak, relative to the highest power, to still be considered a peak. For example, for LSST, if the highest peak's power was 0.8, then the peak power cutoff would be 0.08. "L-S Peak Order" is the "order" argument to the `argrelmax` function in scipy/cuSignal.

0, where σ is the standard deviation of all the powers in the window periodogram, a peak. The LSP peaks were found using the `argrelmax` function in SciPy/cuSignal [53, 66], which has a time complexity Ψ of $O(om)$ where m is the number of frequencies examined and o is the `order` parameter. The `order` parameter for `argrelmax` and the minimum peak height, relative to the strongest peak, is located in Table 2.3.

2.4.4 VanderPlas (VP) Method

VanderPlas [63] describes a method for removing aliases that also utilizes the window function. The difference between this method and the window method is that it compares more peaks between the LSP and window periodogram and in particular it considers pseduo-aliases.

The VP method steps are as follows, where $f_{\text{peak}} = \max(P(f))$:

1. Check if there are any peaks in the LSP at f_{peak}/m, where $m \in \{2, 3\}$ which checks if the found peak is an integer multiple of the real peak.

2. Check for peaks at $f_{\text{peak}} \pm n\delta f$, where $n \in \{1, 2\}$ and where δf is the frequency having the highest window periodogram power.

3. Manually check the highest peaks and fit a model to find the best one. We ignore this step as this requires human intervention, which is not feasible for large-scale survey data.

This method has the same time complexity as the window method at $O(nm) + \Psi$, where Ψ, when using `argrelmax`, is $O(om)$ and it shares its **advantages** and **disadvantages** since the methods are similar. The implementation also uses the same parameters as the Window method, located in Table 2.3.

2.5 Results

All L-S and window functions used the implementations from SciPy/cuSignal, using 5×10^6 frequencies on a uniform period grid on $[1\,\mathrm{h}, 150\,\mathrm{h}]$.

As a baseline, Figure A.2 shows the period distribution when no dealiasing is applied and Figures A.3–A.6 shows the period distributions for the four methods presented above. Figure A.7 also shows the evolution of SSPDB's period distribution over time.

Each of the distributions has spikes at aliases, meaning that none of the approaches are completely successful at removing all aliases because we assume that the true period distributions for our population are continuous .

Our next step is to compare the derived results with known values. For ZTF period solutions, the known values are provided by the LCDB (Section 2.4.1), which contains few alias solutions because of human curating and/or observational cadence that do not have aliasing at the derived periods. There are 2544 objects that are in both the LCDB and ZTF; all of them were used for the calculations. For the SSPDB, since we assigned rotation periods for every object, verifying the correct periods in aliased and de-aliased solutions for this case is straightforward.

The percentage match between the derived period and the real period is shown in Table 2.4. Objects were considered to have matching periods if their period, half their period, or double their period was within 10% of the LCDB (for ZTF) or assigned period (for SSPDB). The baseline method for both surveys had a match rate of over 50%, so most objects have their correct period derived. Once the methods were applied, the masking and window methods increased the match percentage over the baseline for both surveys while the MC

Method	Percentage Match		Percentage Change	
	ZTF	SSPDB	ZTF	SSPDB
None/Baseline	64.8%	57.9%	—	—
Mask	65.8%	74.5%	1.56%	28.6%
MC	70.1%	53.5%	8.08%	−7.61%
Window	69.0%	71.5%	6.39%	23.4%
VP	14.0%	8.91%	−78.4%	−84.6%

Table 2.4: The percentage match between the derived period and the real period for the three surveys and the percentage change from the baseline. The "None/Baseline" row is when none of the methods were used and the highest LSP power was used as the derived period. SSPDB used a sample of 10,000 objects.

method only increased the match percentage for ZTF, and the VP method decreased the match percentage for both surveys.

2.6 Discussion

We begin by examining ZTF and excluding the VP method (which will be described later). The best match percentage using ZTF is with the MC method; however, all of the methods are within $\approx 6\%$ of each other, including the baseline. At a minimum, if de-aliasing is needed for a ZTF-like survey, the masking method should be implemented as it incurs no extra cost. If computational cost is not prohibitive, then the MC should be implemented. In all cases (except where VP is implemented), our results suggest that around two-thirds of all reported solutions are likely to be correct.

For SSPDB, the variation among non-VP approaches is greater than for ZTF, ranging from barely better than 50% (MC) to almost 75% accurate (masking). Notably, the MC method performs worse than the baseline. We first hypothesized that the long baseline of the SSPDB observations leads to the points in each subsample being too temporally distant[6] for L-S to reliably derive the correct period. There is some evidence of this, because when only three years of SSPDB data is used, the overall match percentage increases from 52.8%

[6]This is only an issue for the MC method. Having a long baseline of observations is beneficial for the other methods.

to 53% when using the MC method. This increase is not as large as ZTF's MC increase and it could be argued that the 0.2% increase is not significant, so our initial hypothesis could be wrong and the difference in MC's performance is the result of ZTF's and SSPDB's cadence and/or data quality being different.

The VP method was the worst performing of the methods as it seems to incorrectly select aliases/pseudo-aliases, causing the method to "overcorrect". Figure A.6 shows that there are regions where no periods are detected and periods tend to be derived at longer periods, meaning that the correct periods get derived a small percentage of the time. With the VP and window methods being similar, we hypothesize that the reason the VP method is worse is that the pseudo-alias check causes an overcorrection of the periods.

One may wonder whether the match percentages found here could be improved since all of the methods still have derived periods at or near aliases. It is possible that better parameters for the methods could be found with a more exhaustive search of the parameter space, like those in Table 2.3. However, such a search is impractical due to the large volume of data in the catalogs.

For the masking method, since it is static and therefore unable to react to changes in aliases, the masks might have to be re-derived after the survey starts if an inaccurate simulation was used or if the observational cadence of the survey changes during the survey.

One important conclusion is that the best de-aliasing approach is not the same for ZTF and SSPDB, which implies that a study like this should be carried out for every large-scale survey. If this is impractical and a single uniform approach is preferred, we identify the masking process as the most effective, though this conclusion is based only on the two data sets considered here.

2.7 Conclusions and Future Work

We used two sets of survey data, one real and one synthetic, to test four de-aliasing techniques for period solutions from all-sky surveys.

We find that the masking method provides the overall best results and should be chosen for any given survey. This method has a relatively low time complexity. The masks for ZTF and SSPDB, and therefore LSST, have been generated and are presented in Table 2.1. The window method would also be a good choice to apply if the computational performance loss compared to the masking method is not important as it provides aliases for each object individually. However, we note that results may vary from survey to survey, and the best approach is to carry out individualized studies, such as this one.

This paper leads to several lines of future investigation:

- Improving the window method so it provides a higher match rate.
- Use several of the methods together to see if that improves the match rate.
- Develop a GPU version of the MC method in order to decrease its expensive computation time.
- Develop a method that removes the pseudo-aliases.
- Test how differences in a survey's simulated data and its real data change its mask ranges.
- Develop and test methods for determining a "confidence" in a periodogram result in order to better gauge if a derived period result is correct.

2.8 Acknowledgements

We acknowledge many useful conversations with Nat Butler and John Kececioglu and with Tom Matheson and the ANTARES team. This work has significantly benefited from all of their expertise.

This work has been supported in part by the Arizona Board of Regents, Regents' Innovation Fund.

ZTF is a public-private partnership, with equal support from the ZTF Partnership and from the U.S. National Science Foundation through the Mid-Scale Innovations Program (MSIP). The ZTF partnership is a consortium of the following universities and institutions (listed in descending longitude): TANGO Consortium of Taiwan; Weizmann Institute of Sciences, Israel; Oskar Klein Center, Stockholm University, Sweden; Deutsches Elektronen-Synchrotron & Humboldt University, Germany; Ruhr University, Germany; Institut national de physique nucléaire et de physique des particules, France; University of Warwick, UK; Trinity College, Dublin, Ireland; University of Maryland, College Park, USA; Northwestern University, Evanston, USA; University of Wisconsin, Milwaukee, USA; Lawrence Livermore National Laboratory, USA; IPAC, Caltech, USA; Caltech, USA. We thank the anonymous reviewer for their insightful comments and helpful feedback on our manuscript.

Chapter 3

The Effect of Different LSST Cadences on Derived Rotation Periods for Solar System Small Bodies

Daniel Kramer[12], Michael Gowanlock[12], David Trilling[21]

Submitted to The Astronomical Journal *on 2023-03-30.*

3.1 Introduction

Upcoming large-scale astronomical surveys, like the Legacy Survey of Space and Time (LSST, Ivezić et al. [32]), will produce a vast trove of sparse astronomical data. LSST will observe around 40 billion sources over 10 years; around 5 million of these will be from small bodies in the solar system. All small bodies have some physical rotation period and correctly determining its period provides important for understanding he origin and evolution [11, 12, 56] and the physical properties [44] of the object.

Determining an object's rotation period is one of the most challenging problems large scale surveys pose to small body astronomy. The main cause of incorrect periods is the sparse observing of objects/fields of these surveys, along with the day-night cycle of the Earth [36, 63]. This causes aliasing and pseudo-aliasing, effects where the cadence of a survey injects an incorrect signal into the rotation period periodogram— the signal strength

[1]School of Informatics, Computing, and Cyber Systems, Northern Arizona University, Flagstaff, AZ 86011, USA

[2]Department of Astronomy and Planetary Science, Northern Arizona University, Flagstaff, AZ 86011, USA

of angular frequencies that appear in a time-series.

Part of the current LSST development is determining an observing strategy that maximizes the science results of different research areas [40]. In order to accomplish this, LSST Science Collaboration et al. [40] and members of the greater scientific community created different types (families) of observational cadences. Simulations of LSST observations using these families were then generated, refined, and then generated again. At the time of this writing, version `v3.0` has been released, bringing the total number of simulations[3][4] to 602.

In order to test the simulations, the Metrics Analysis Framework (MAF, Jones et al. 33) was created. Its purpose was to test the effectiveness of a simulation for many different science cases. However, none of the science cases MAF addresses study the impact of different cadences on deriving small body rotation periods. This paper addresses this deficiency injecting synthetic asteroids into the LSST cadences and measuring the effectiveness of deriving rotation periods in each cadence.

This paper is organized as follows: Section 3.2 describes the methods used to generate and process the simulations, Section 3.3 discusses the results from the simulations, Section 3.4 provides our discussion of the results of the paper, and Section 3.5 presents our conclusions.

3.2 Methods

The three main steps in obtaining synthetic asteroid rotations from a simulation were obtaining the simulations (Subsection 3.2.1), generating synthetic observations (Subsection 3.2.2), and generating rotation periods from the observations (Subsection 3.2.3).

3.2.1 Simulated LSST cadences

The LSST cadence simulations are stored at `http://astro-lsst-01.astro.washington.edu:8081/` and `http://astro-lsst-01.astro.washington.edu:8080`. Seven different fam-

[3] `http://astro-lsst-01.astro.washington.edu:8081/`
[4] `http://astro-lsst-01.astro.washington.edu:8080`

ilies characterize the simulations:

- Baseline: This family contains baseline simulations, which all the other simulations are built on. The properties of this family can be found the the notebook linked below. This family has 3 simulations.

- Deep Drilling Field (DDF): This family has dedicated observing times in which certain predetermined fields (the Deep Drilling Fields; DDFs) are observed continuously with some interjection of the "normal" fields. When not targeting a DDF, this cadence follows the baseline simulation. This family has 92 simulations.

- Good Seeing: This family has at least three images per year with $< 0.8''$ seeing with certain filters. This family has 14 simulations.

- March Start: This family starts in March 2023 instead of an October 2024 start. This family has 1 simulation.

- No Repeat: This family suppresses repeat observations to fields that have already been observed that same night. This family has 6 simulations.

- Galactic Plane Footprint: Compared to the baseline, this family observes more fields on the galactic plane than in the galactic bulge. This family has 16 simulations.

- Varying Exposures: This family varies the exposure time of each image from the baseline of 30 sec. This family has 9 simulations.

More information on the families and their subfamilies can be found at `https://github.com/lsst-pst/survey_strategy/blob/main/fbs_2.0/SummaryInfo_v2.1.ipynb`.

All simulations are appended by their version number and the length of the simulations (i.e. the string `_2.1_10yrs` appended at the end of a simulation name means it is a `v2.1` simulation that spans ten years). Since all of the simulations examined here are ten years in length, in this paper we omit this part of the simulation name, for brevity. The `v2.1` simulations have also had their version number omitted in this paper.

It should be noted that all LSST simulations follow the general "wide fast deep" approach, meaning that, in the absence of programmatic requirements as described above, fields are prioritized to minimize airmass, slew time, and other inefficiencies in a nightly survey program.

3.2.2 Injecting synthetic Solar System objects

For a population of objects, we used the Pan-STARRS Synthetic Solar System Model (S3M; Grav et al. 27). S3M provides a list of 4.33×10^6 objects, their orbital parameters, and some physical properties, like absolute magnitude in different filters.

The following steps were carried out to generate small body observations for each simulation:

1. 15,000 objects were randomly sampled from S3M. 15,000 was chosen to provide a large statistical sample of objects while not taking a "long" time for the following steps to compute.

2. These objects, along with the cadence being examined, were used as input for Objects In Field[5] (`oif`), which calculates the orbits of the objects and determines which objects are in the field of view in each simulated "image" of the telescope. For this step we used a fork[6] of `oif` that implemented an improved interface to call `oif` from other Python[7] code.

3. We used `surveysimPP`[8] to augment the `oif` output by calculating photometric error, adjusting the observed magnitude of the object based on its size, and imposing the field's magnitude limits. We used a fork[9] of `surveysimPP` that implemented an improved interface to call `surveysimPP` from other Python code.

[5] `https://github.com/AsteroidSurveySimulator/objectsInField`
[6] `https://github.com/drk98/objectsInField`
[7] `https://www.python.org/`
[8] `https://github.com/dirac-institute/survey_simulator_post_processing`
[9] `https://github.com/drk98/survey_simulator_post_processing`

4. The objects generated from `oif` and `surveysimPP` do not have shape-induced rotational light-curves. We used the Light Curve Database (LCDB, Warner et al. [68]) period distribution and an amplitude distribution with a gamma distribution implemented from SciPy [66], and the parameters $a = 0.48$ and $\frac{1}{\beta} = 0.18$ to assign each object with a light-curve. The maximum period allowed was 500 h and the minimum amplitude allowed was 0.1mag.

5. The absolute magnitude for each observation was then generated using phase_curve_tools[10].

6. All of the observational data is stored in a MongoDB[11] collection for each simulation.

3.2.3 Period Derivation

Our next step is to derive the rotation period for each object in each simulation. We used the Lomb-Scargle Periodogram (LSP, Lomb [38], Scargle [57]) approach implemented with GPU Lomb-Scargle [24]. The mean magnitude of each filter's observations was subtracted from the filter's observations. This set the mean magnitude of each filter to 0. The filter's data was then concatenated together to create a single band of data with a mean magnitude of 0. The periodogram was then computed on this single band of data on a even frequency range $\frac{1}{500}\,\mathrm{h}^{-1}$ to $1\,\mathrm{h}^{-1}$ with 5×10^6 frequencies.

The highest power from the periodogram was used as the derived period and was then stored in a sister MongoDB collection to the simulation's output collection.

3.3 Results

There were 141 simulations used, 139 from the `v2.1` simulations and the two `v1.7`/`v1.7.1` baseline simulations. Over all of the 141 simulations, there were 3.935×10^8 observations, corresponding to about 2.791×10^6 observations per simulation. The `v1.7`/`v1.7.1` baselines

[10] `https://github.com/drk98/phase_curve_tools`
[11] `https://www.mongodb.com/`

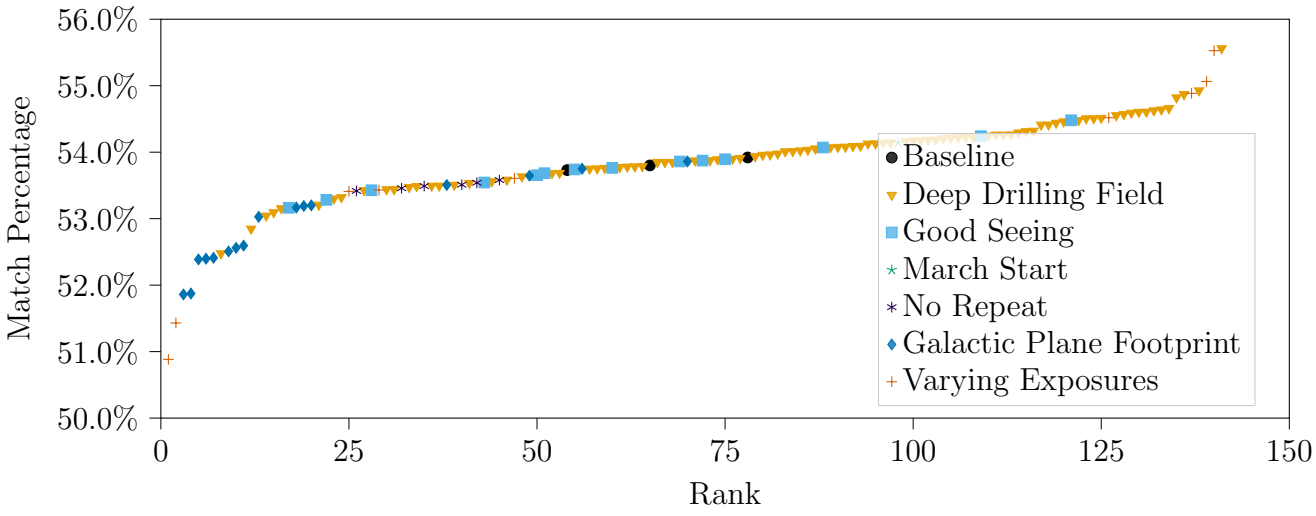

Figure 3.1: The match percentage for each of the 141 simulations. The x-axis is the simulation's match percentage ranking ordered from lowest to highest. The y-axis is the match percent for the simulation. Each simulation family is marked.

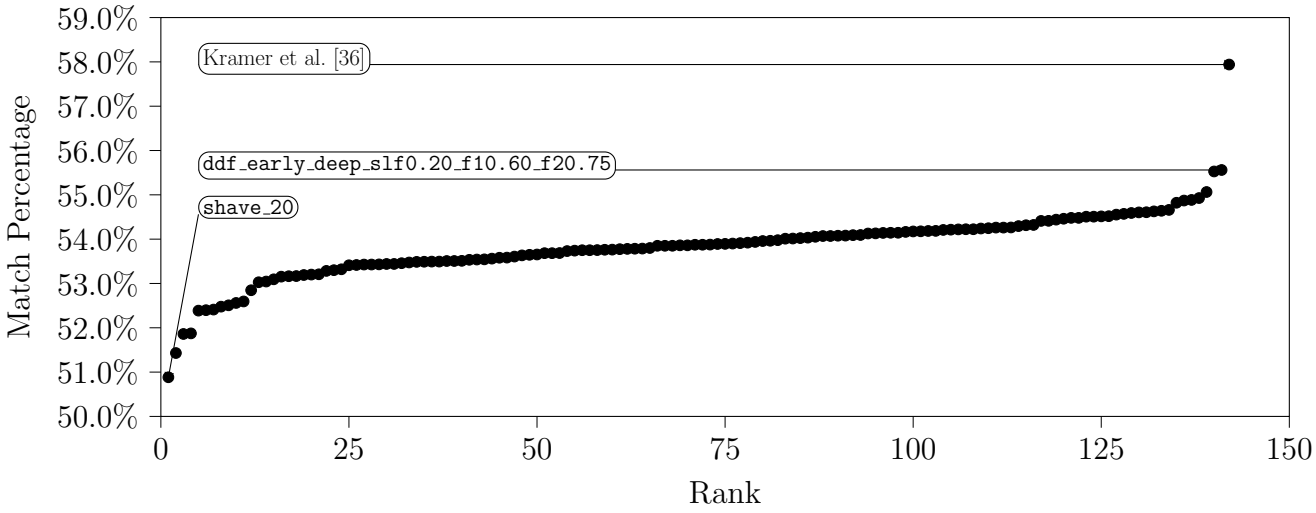

Figure 3.2: The same as Figure 3.1, but with the best and worst rank labeled. The de-aliased result from Kramer et al. [36], which used the LSST Solar System Product Database (SSPDB), is added for comparison.

were included as comparisons for the `v2.1` baseline and the results from Kramer et al. [36], which are discussed further in Section 3.3.1.

3.3.1 Total Match Rate

In order to determine which simulation is the best at correctly deriving asteroid periods, the match percentage between the derived period and the assigned period is calculated. A derived period within 5% of the object's assigned period was considered correct. The match percentage for each simulation is presented in Table 3.1.

All simulations are within 4.68% of each other — a relatively small range of results — with a mean match percentage of 53.81%. Simulation `ddf_early_deep_slf0.20_f10.60_f20.75` had the best match rate with 55.56% and `shave_20` had the worst with 50.88%.

Figure 3.1 shows the match percentages of each simulation from Table 3.1 as a function of rank, where each major family has the same color/symbol. This figure shows that, on average, the DDF (Deep Drilling Fields) family has the greatest match percentage of the seven families. It also shows a dichotomy in the Varying Exposure family, where the long exposure simulations have a high match percentage and the short exposures have a low match percentage.

Kramer et al. [36] carried out an analysis of several de-aliasing approaches that can be used when deriving asteroid rotation periods (or other regular periodic behaviors). For one of their datasets, they used the LSST Solar System Product Database (SSPDB, Juric et al. [34]), the official LSST asteroid simulation; SSPDB is based on `baseline_nexp2_v1.7.1`, which was included in this analysis.

All of the match percentages presented here are less than the baseline results from Kramer et al. [36], which has a match rate of 57.9% (Figure 3.2). The match percentage for `baseline_nexp2_v1.7.1` presented here — straight from the observations — is 4.14% less than the baseline result presented in Kramer et al. [36]. This discrepancy is discussed more in Section 3.4.

3.3.2 Match Rate Over Time

The observational record for each simulation allows us to determine the behavior of each simulation in terms of match percentage and observation count over the ten year lifespan of LSST.

To accomplish this, the simulation with the match percentage closest to the family's mean match percentage was chosen:

- `shave_35`
- `shave_25`
- `baseline_nexp2_v1.7.1`
- `ddf_quad_slf0.10`
- `good_seeing_gsw0.0`
- `no_repeat_rpw-20.0`
- `plane_priority_priority0.3_pbt`

The March Start family was not included because of its similarity to the baseline simulations. The Varying Exposures family was split into its low match percent and high match percent families because of the clear dichotomy in those two groups ($[50.58\%, 53.61\%]$ and $[54.52\%, 55.53\%]$, respectively). We are assuming that each of the simulations in a family will have approximately the same match rate over time.

For these seven simulations, periods were derived, as described in Section 3.2.3, for all the observations up to the end of year 1, the end of year 2, etc. Figure 3.3 shows the each year's match percent, normalized to its year ten match percentage. This figure shows that, without a minimum observation cutoff, no simulation will obtain $> 40\%$ of its year ten match percentage in year one. Also, none of the match rates plateau, meaning that, if LSST were to go for longer than ten years, higher match rates could be achieved.

Figure 3.4 is similar to Figure 3.3, but with the requirement that each object in the simulation had to have > 50 observations to be included. This figure shows that, with a 50 observation minimum, most simulations recover $90\% - 95\%$ of their final match rate at year 1. Two simulations also started at a greater match rate in year one (and only in year 1) than in year 10 (this unexpected results is discussed in Section 3.4). In this case (as in Figure 3.3), the match rate does not plateau so higher match rates could be achieved if LSST had a longer baseline.

Figure 3.5 shows box and whisker plots of the number of observations over time. This figure shows that the non-Varying Exposure simulations have about the same median number of observations and about the same maximum number of observations as each other. Simulation `shave_25`, which has 25 sec exposures, has the highest median and highest maximum number of observations (except for one object from Good Seeing) while simulation `shave_35`, which has 35 sec exposures, has the lowest median and lowest maximum number of observations.

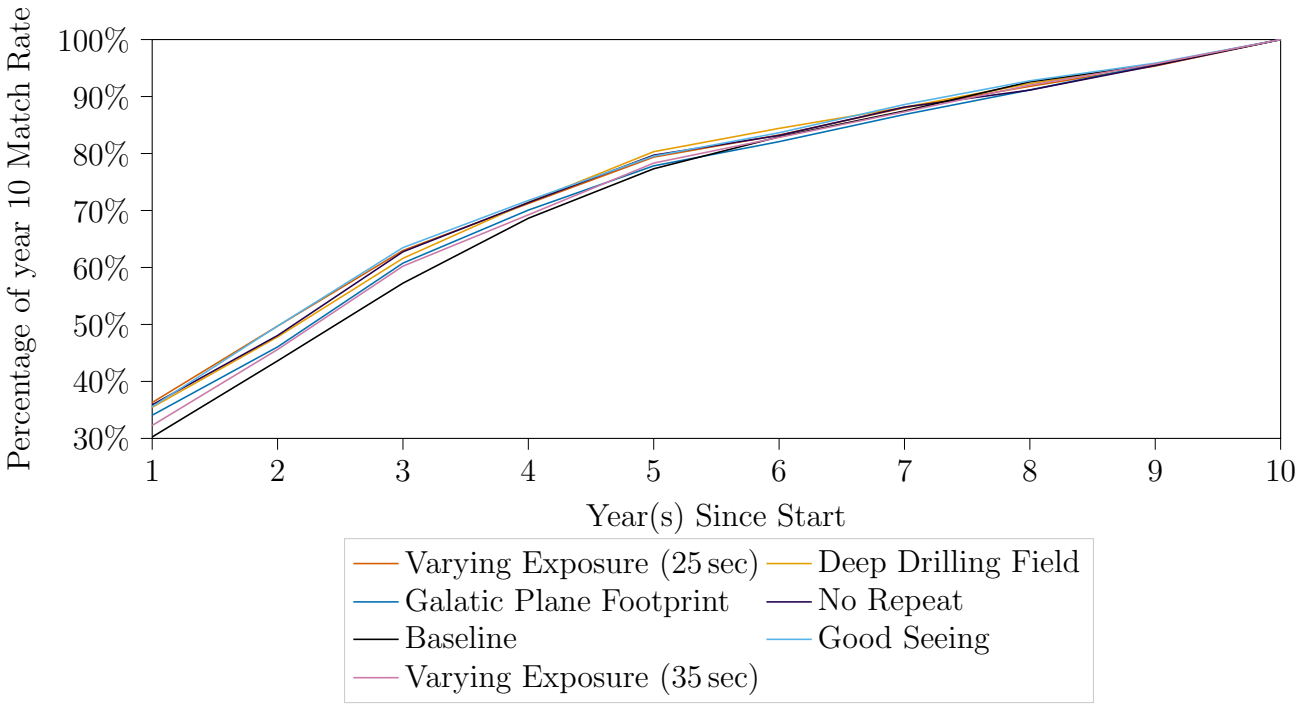

Figure 3.3: The overall percentage of the year ten match rate for the average families in each simulation. The x-axis is the year and the y-axis is the percentage of the year ten match rate.

No.	Simulation Name	Match (%)	No.	Simulation Name	Match (%)	No.	Simulation Name	Match (%)
1	ddf_early_deep_slf0.20_f10.60_f20.75	55.56	48	ddf_accourd_sf0.10_lsf0.3_lsr0.5	54.13	95	shave_32	53.61
2	shave_40	55.53	49	ddf_accourd_sf0.10_lsf0.3_lsr0.3	54.09	96	ddf_quad_slf0.20	53.58
3	shave_35	55.06	50	ddf_dither_size_slf0.20_md0.50	54.09	97	no_repeat_rpw-10.0	53.58
4	ddf_quad_subfilter_slf0.35	54.93	51	ddf_bright_slf0.30	54.08	98	ddf_accourd_sf0.25_lsf0.4_lsr0.1	53.56
5	shave_38	54.88	52	ddf_accourd_sf0.05_lsf0.4_lsr0.1	54.08	99	good_seeing_gsw1.0	53.54
6	ddf_early_deep_slf0.20_f10.60_f20.70	54.87	53	ddf_accourd_sf0.25_lsf0.3_lsr0.1	54.07	100	no_repeat_rpw-1.0	53.54
7	ddf_early_deep_slf0.20_f10.60_f20.80	54.82	54	good_seeing_u_gsw20.0	54.07	101	ddf_accourd_sf0.10_lsf0.2_lsr0.3	53.53
8	ddf_accourd_sf0.10_lsf0.1_lsr0.3	54.66	55	ddf_accourd_sf0.10_lsf0.2_lsr0.5	54.05	102	no_repeat_rpw-100.0	53.51
9	ddf_double_slf0.35	54.64	56	ddf_quad_subfilter_slf0.10	54.03	103	ddf_bright_slf0.20	53.51
10	ddf_accourd_sf0.10_lsf0.2_lsr0.1	54.63	57	ddf_quad_slf0.15	54.02	104	plane_priority_priority0.9_pbt	53.51
11	ddf_accourd_sf0.05_lsf0.2_lsr0.3	54.61	58	ddf_dither_size_slf0.20_md0.25	54.01	105	ddf_season_length_slf0.10	53.49
12	ddf_quad_subfilter_slf0.25	54.60	59	ddf_quad_slf0.10	54.01	106	ddf_accourd_sf0.10_lsf0.4_lsr0.5	53.49
13	ddf_deep_rolling_slf0.20	54.59	60	ddf_accourd_sf0.30_lsf0.4_lsr0.1	53.98	107	no_repeat_rpw-20.0	53.49
14	ddf_season_length_slf0.15	54.57	61	ddf_accourd_sf0.10_lsf0.3_lsr0.1	53.96	108	ddf_bright_slf0.25	53.49
15	ddf_accourd_sf0.30_lsf0.4_lsr0.5	54.55	62	ddf_accourd_sf0.05_lsf0.3_lsr0.3	53.96	109	ddf_double_slf0.25	53.47
16	shave_30	54.52	63	ddf_accourd_sf0.20_lsf0.3_lsr0.5	53.94	110	no_repeat_rpw-2.0	53.46
17	ddf_accourd_sf0.05_lsf0.2_lsr0.5	54.51	64	baseline_nexp2_v1.7	53.92	111	ddf_bright_slf0.10	53.44
18	ddf_dither_size_slf0.20_md0.10	54.51	65	ddf_accourd_sf0.20_lsf0.4_lsr0.3	53.91	112	ddf_dither_size_slf0.20_md0.70	53.44
19	ddf_accourd_sf0.05_lsf0.4_lsr0.5	54.51	66	ddf_old_rot_slf0.15	53.90	113	shave_28	53.43
20	ddf_accourd_sf0.25_lsf0.3_lsr0.3	54.48	67	good_seeing_gsw50.0	53.89	114	good_seeing_u_gsw6.0	53.43
21	good_seeing_gsw6.0	54.48	68	ddf_double_slf0.30	53.89	115	ddf_dither_size_slf0.20_md1.50	53.43
22	ddf_accourd_sf0.25_lsf0.3_lsr0.5	54.46	69	ddf_double_slf0.20	53.88	116	no_repeat_rpw-5.0	53.42
23	ddf_accourd_sf0.20_lsf0.4_lsr0.1	54.44	70	good_seeing_u_gsw10.0	53.87	117	shave_25	53.41
24	ddf_accourd_sf0.10_lsf0.4_lsr0.1	54.41	71	ddf_accourd_sf0.20_lsf0.4_lsr0.5	53.87	118	ddf_deep_u_slf0.20	53.32
25	ddf_quad_subfilter_slf0.15	54.41	72	plane_priority_priority0.9_pbf	53.86	119	ddf_accourd_sf0.05_lsf0.1_lsr0.3	53.30
26	ddf_euclid_moved_slf0.20	54.32	73	good_seeing_u_gsw1.0	53.86	120	good_seeing_gsw20.0	53.28
27	ddf_accourd_sf0.20_lsf0.3_lsr0.3	54.31	74	ddf_accourd_sf0.25_lsf0.4_lsr0.3	53.85	121	ddf_dither_size_slf0.20_md3.50	53.21
28	ddf_old_rot_slf0.10	54.29	75	ddf_season_length_slf0.20	53.85	122	plane_priority_priority0.6_pbf	53.20
29	ddf_quad_slf0.35	54.26	76	ddf_quad_subfilter_slf0.30	53.85	123	pencil_fs2	53.19
30	ddf_accourd_sf0.25_lsf0.4_lsr0.5	54.26	77	baseline_nexp2_v1.7.1	53.80	124	plane_priority_priority0.6_pbt	53.17
31	ddf_accourd_sf0.05_lsf0.3_lsr0.1	54.26	78	ddf_accourd_sf0.20_lsf0.3_lsr0.1	53.79	125	good_seeing_u_gsw0.0	53.16
32	ddf_accourd_sf0.05_lsf0.3_lsr0.5	54.25	79	ddf_dither_size_slf0.20_md2.50	53.78	126	ddf_roll_slf0.20	53.15
33	good_seeing_gsw3.0	54.24	80	ddf_old_rot_slf0.30	53.78	127	ddf_quad_slf0.25	53.09
34	ddf_accourd_sf0.30_lsf0.4_lsr0.3	54.22	81	ddf_season_length_slf0.25	53.77	128	ddf_accourd_sf0.05_lsf0.4_lsr0.3	53.04
35	ddf_accourd_sf0.05_lsf0.1_lsr0.1	54.22	82	good_seeing_gsw0.0	53.76	129	plane_priority_priority0.3_pbt	53.03
36	ddf_accourd_sf0.05_lsf0.1_lsr0.5	54.22	83	ddf_accourd_sf0.10_lsf0.1_lsr0.5	53.76	130	ddf_accourd_sf0.10_lsf0.1_lsr0.1	52.85
37	ddf_accourd_sf0.05_lsf0.2_lsr0.1	54.21	84	ddf_old_rot_slf0.25	53.75	131	plane_priority_priority0.2_pbt	52.59
38	ddf_dither_size_slf0.20_md0.01	54.21	85	ddf_quad_subfilter_slf0.20	53.75	132	plane_priority_priority0.1_pbf	52.56
39	ddf_accourd_sf0.10_lsf0.4_lsr0.3	54.19	86	plane_priority_priority1.2_pbt	53.75	133	plane_priority_priority0.4_pbf	52.51
40	ddf_season_length_slf0.30	54.18	87	good_seeing_u_gsw3.0	53.74	134	ddf_bright_slf0.35	52.48
41	ddf_dither_size_slf0.20_md1.00	54.18	88	baseline	53.73	135	plane_priority_priority0.4_pbt	52.41
42	ddf_quad_slf0.30	54.17	89	ddf_old_rot_slf0.20	53.69	136	pencil_fs1	52.40
43	ddf_old_rot_slf0.35	54.16	90	ddf_bright_slf0.15	53.68	137	plane_priority_priority0.3_pbf	52.39
44	march_start	54.14	91	good_seeing_gsw10.0	53.68	138	plane_priority_priority0.2_pbf	51.87
45	ddf_season_length_slf0.35	54.14	92	good_seeing_u_gsw50.0	53.65	139	plane_priority_priority0.1_pbt	51.86
46	ddf_dither_size_slf0.20_md0.05	54.14	93	plane_priority_priority1.2_pbf	53.65	140	shave_22	51.43
47	ddf_double_slf0.10	54.13	94	ddf_double_slf0.15	53.63	141	shave_20	50.88

Table 3.1: The simulations and their match percentage, ranked by the match percentage.

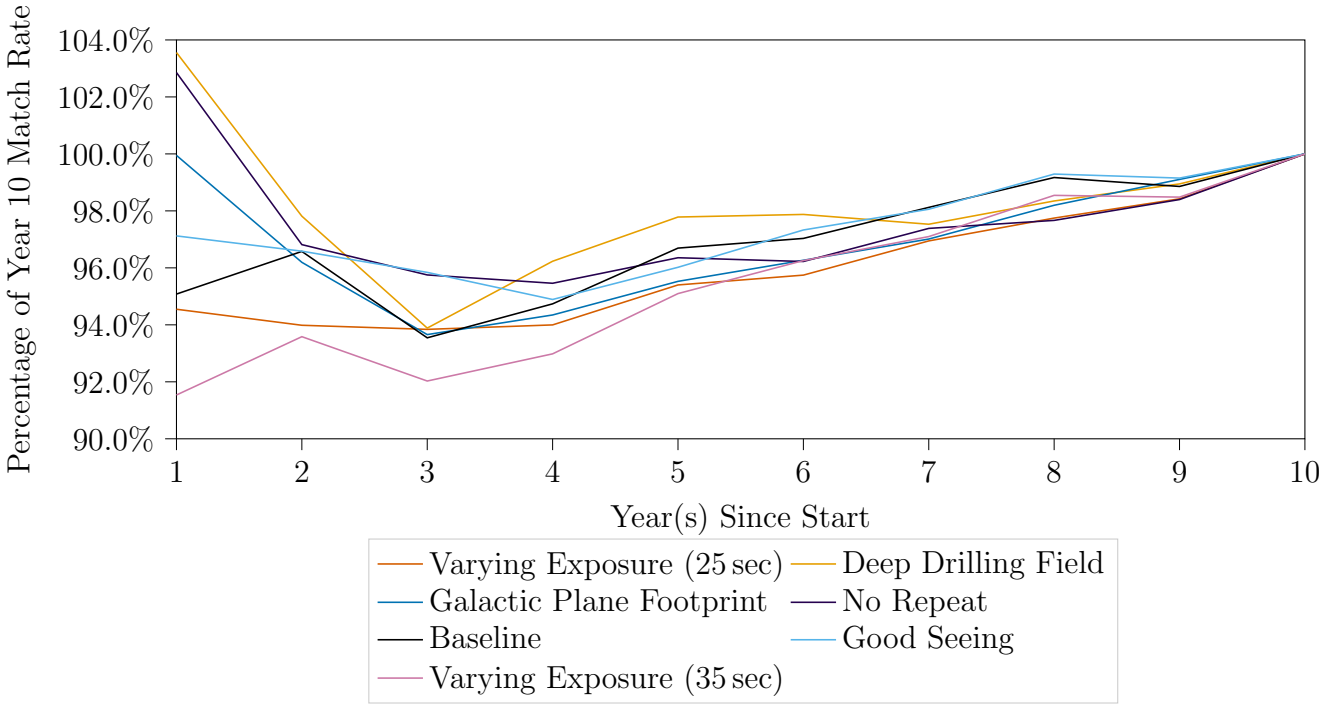

Figure 3.4: The same as Figure 3.3 but with for objects with at least 50 observations.

3.4 Discussion

We begin by looking at the Varying Exposure simulation family, denoted by the + markers in Figure 3.1. There is a correlation between the match percentage and the exposure time, meaning that, all else being equal, longer exposure times correspond to a higher match rate. This is because longer exposure times produce smaller observational errors and therefore higher fidelity solutions. Because the total survey time is fixed, longer exposure times lead to a decrease in the number of observations per object. Therefore, we find that, for period derivation, the accuracy of individual observations is more important than the number of observations, assuming some minimum number of observations (we suggest 50 observations).

We now examine the DDF simulation family, denoted by the ▼ markers in Figure 3.1. Most of the simulations in this family have a match percentage above the overall mean of 53.81%. This is likely because, even though asteroids are not stationary, the LSST field of view is so large, that an asteroid could stay in the field for an extended period of time, so the

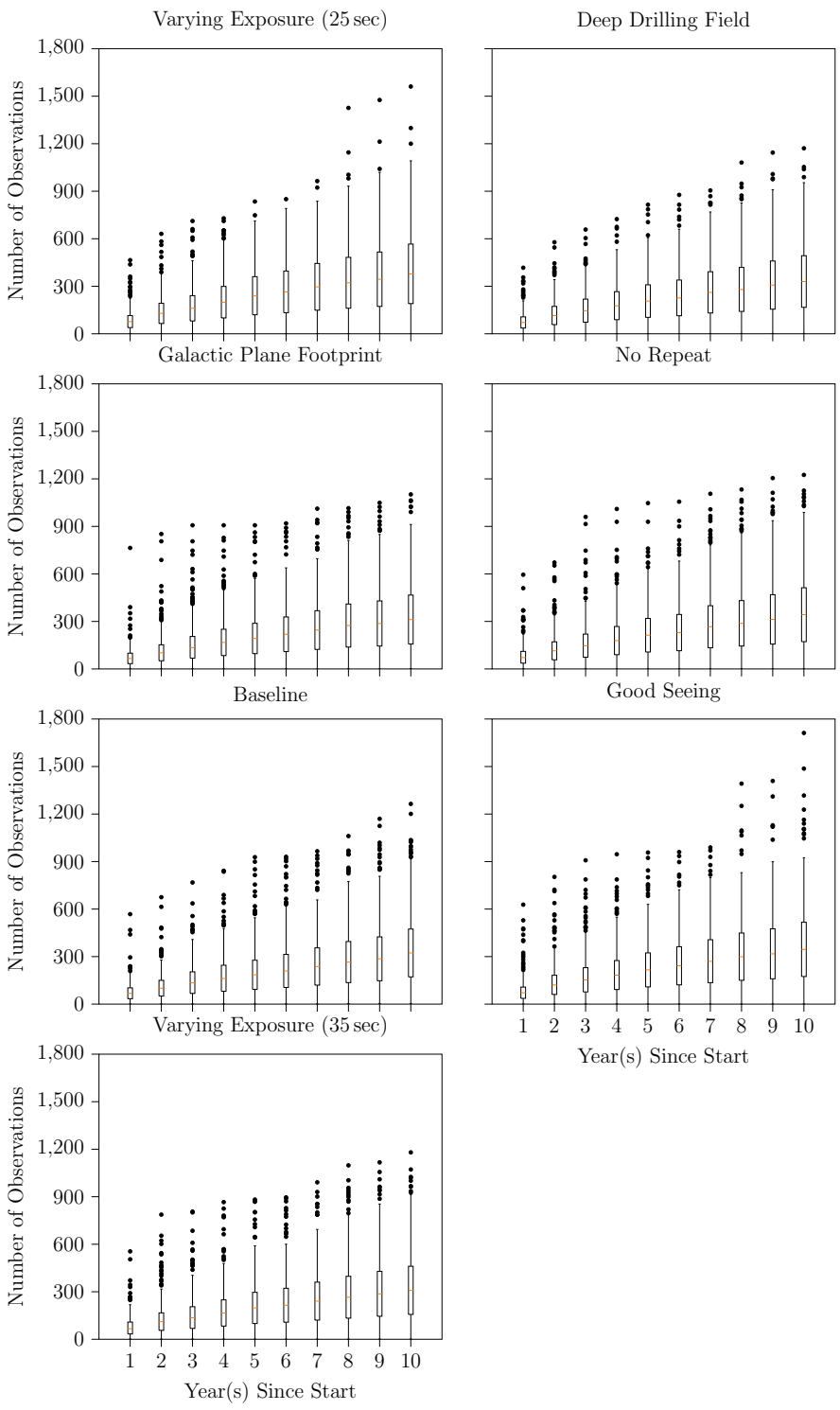

Figure 3.5: Box and whisker plots for the number of observations the average simulation in each family has. For each year, the orange line in each box is the median. The ends of the box are the first quartile (Q1) and third quartile (Q3) of the number of observations. The whiskers go to $\{\text{Q1}, \text{Q2}\} \mp 1.5 \times (\text{Q3} - \text{Q1})$ or the minimum/maximum of the data, whichever comes first. The dots past the whiskers are outlier points.

object is consistently observed. Constant observations causes a LSP to approach its limiting case of being a Discrete Fourier transform [63], so accurate periods can be derived. It should also be noted that some of the DDF simulations under-preform and more work needs to be done to explain why.

Conversely, the No Repeat simulation family, denoted by the $*$ markers in Figure 3.1 and which is designed to not have repeat visits of a field in a night, has a low match rate. These two results (DDF and No Repeat) suggest period determinations for small bodies are improved when there is a small time difference between adjacent observations. (This cadence also improves the recovery rate of new asteroids [40].)

The match percentage over time (Figures 3.3 and 3.4) shows that some cutoff for number of observations is needed if periods are to be accurately derived early in the LSST survey. Interestingly, the DDF and No Repeat simulation have higher match rates at year one than year ten. The most likely cause for the DDF was because of more DDFs present in year 1 than the average yearly rate. Overall, DDF observations in general are beneficial to small body period solutions. It is unknown as to why the No Repeat simulations has $> 100\%$ in year one.

The difference between our `baseline_nexp2_v1.7.1` and Kramer et al. [36], which both used `baseline_nexp2_v1.7.1`, is most likely because we used an updated version of `oif` and/or the post-processing did not use the same parameters (it is unknown the exact post-processing steps and parameters SSPDB used). Therefore, the 4.14% difference between `baseline_nexp2_v1.7.1` and Kramer et al. [36] means all of our results could be 4.14% less than their real value. This may suggest an overall systematic shift of our derived match rates. The relative differences from each simulation should remain the same (i.e. `shave_40` will always have a better match percentage than `pencil_fs1`).

3.5 Conclusions and future work

We used 141 different, official LSST simulations in conjunction with two software tools to calculate realistic LSST observations for asteroids. Rotations were then assigned to these objects and then their periods derived. For each simulation, and for families of simulations, we calculated the percentage of input periods that were derived correctly: the match percentage. The total range of match percentage spanned 50.88% to 55.56% with the baseline simulations being about average.

We found that the simulations that had long(er) exposure times, and therefore fewer observations, and simulations that had consistent observations of the same field (the Deep Drilling Field family of simulations) had the greatest match percentage. Future surveys for which deriving periodic solutions — especially for moving objects — is an important goal would benefit from high fidelity (signal to noise) measurements and campaigns that target a single field. DDF-like programs produce a high match rate for a relatively limited number of small bodies.

We find that the match rate increases over time for every simulation family, and that is has not plateaued by year ten, suggesting that an even longer survey would continue to increase the number of accurate period solutions. However, the match rate starts and stays high when the number of observations per object is required to be 50 or more.

This paper leads to several lines of future investigation:

- The same analysis could be carried out for stellar and non-sinusoidal light curves to calculate the match percentage for the stationary objects.
- Analysis on deriving a match percentage for a simulation without having to do perform the computations of simulating small bodies and deriving their periods.
- Investigate why the No Repeat family has a higher match rate in year one than year ten, and whether that implies something systematic about survey success.

- Compare actual LSST performance after year 1 of the survey to determine the performance of the survey compared to these expected results.

3.6 Acknowledgements

The source code for this project is available at `https://github.com/drk98/cadence-alias-effects`.

We thank Samuel Cornwall and Siegfried Eggl for their help with `Objects in Field` and `SurveySimPP`.

This work has been supported in part by the Arizona Board of Regents, Regents' Innovation Fund.

`Objects In Field` is powered by matplotlib [31], numpy [28], openOrb [26], pandas [50, 69], SPICE utilities [1, 2], and scipypy [3].

`SurveySimPP` is powered by astropy [4, 5, 6], matplotlib [31], numpy [28], pandas [50, 69], sbpy [46], and scipypy [3].

The colors used in the plots and other parts of this paper uses the Wong color pallet and its extensions (Wong 70; `https://davidmathlogic.com/colorblind/`).

Chapter 4

Conclusion

In order to improve the accuracy of the derivation of small body rotation periods, we examined two major objectives: (1) removing aliases after a survey has taken observations and (2) constructing surveys to have the maximum period match rate.

In *Removing Aliases in Time-Series Photometry* (Chapter 2) four methods were tested in order to determine the best one for removing aliases. Using ZTF and SSPDB data, we found that the window method, where the peaks from the window function are used to remove alias peaks in a LSP, and the masking method, ignoring certain period ranges in a LSP, improved the period match rate the most. The MC method was able to improve the match rate for "short" time baselines (ZTF) and it decreased the match rate for "long" time baselines (SSPDB). Finally, the VP method reduced the match rate in both surveys.

In *The effect of LSST cadences on derived rotation periods for small Solar System bodies* (Chapter 3) 141 official LSST simulations were used to determine the best observing strategy for deriving small body rotation periods. Using two software packages, `Objects in Field` and `surveysimPP`, the simulations "observed" small bodies and then they had rotations applied. We found that simulations with long exposures and dedicated observing of a field resulted in a high match percentage. A byproduct of simulations with long exposures is that they had a fewer number of observations per object, so highly accurate photometry is more important to period derivation than more observations. We also found that the match rate over time did not plateau, so a longer survey would have resulted in a higher match rate.

Overall, there was no way of deriving small body rotation periods with 100% accuracy. While the match rate was able to be improved, more work needs to be done to improve match rates. Sufficed to say, ZTF, LSST, and future all sky surveys will greatly improve our knowledge of small bodies and, using the techniques of astroinformatics, the work done here will aid in understanding their physical properties.

4.1 Future Work

The work in this thesis leads to several lines of questions, in no particular order:

- **Develop methods for removing pseudo-aliases**. None of the work presented here addresses pseudo-aliases, but they are the next largest source of error that can be removed. The pseudo-aliases also directly relate to the period of the object, so removing pseudo-aliases might have the best match percentage. The work that does this should also propose a better name than "pseudo-aliases".

- **Develop a "confidence" metric for period solutions**. As of now, the periods we derive are all treated with the same confidence, but through some analysis, some solutions are look "better" than others, so some metric might be able to capture how good a solution is.

- **Testing the de-aliasing methods and the effects of cadence on period derivation on stellar and non-sinusoidal sources.** L-S is not the best at deriving periods for stellar and non-sinusoidal sources, so the methods used in this thesis should be tested on them.

- **Analyzing the difference between the real LSST period results and the synthetic results.** Once LSST has completed, being able to tell how accurate simulations are would help future surveys derive more accurate simulations.

- **Test different period finding algorithms to find the best algorithm in terms of speed, space required, accuracy, and ability to be de-aliased.** I used L-S as my period finding method, but there might be a better one to use for small bodies when using the aforementioned metrics.

- **Analyze how an object which has had its period changed affects period finding algorithms. For objects with periods changed by a collision, can the time (or a range of time) of the collision be found?** Period changers if a field of research that has had little to no work done, so determining how L-S (or other period finding methods) periodograms change would be important to know.

- **Analyze how changes to the surface of the object (color changing, outgassing/becoming active) affect a period finding algorithm's ability to accurately derive periods.** Similar to the last point, how does a LSP change with an altered surface of an object.

- **Test how much the Phase-Amplitude effect [41] reduces the accuracy of period finding algorithms over long baselines.** Since the Phase-Amplitude effect changes the brightness we observe in a way that phase curve correction does not correct for, the effect on deriving periods can be significant. Determining when this effect is large, and therefore should be accounted for, could greatly increase the match percentage of surveys.

- **What is the slowest rotating small body?** Erasmus et al. [20] only searched to 5000 h but there could be slower objects.

- **What is the fastest rotator an all sky survey like ZTF and LSST could possibly detect?** This value is probably related to Shannon [58], but it is unknown for uneven sampling what the limit is. Also, at a certain point, the error in time (since exposures are not instantaneous) and the exposure being over a large part of the

rotational phase would need to be taken into account.

- **How much does combining data from multiple surveys improve the period match rate?** Could a space-based survey be replicated on Earth with having telescopes where at least one is observing? The ATLAS survey is preparing to do exactly this, but if heterogeneous surveys are used, analysis would have to be done on how different filter sets and data quality affects the combination of the surveys.

- **What is the best way to distribute derived rotation periods (and other derived properties) to the general public?** The LCDB publishes a compiled list as a CSV file every few months and I have developed `rc.nau.edu/snaps` for SNAPS [62] derived data.

- **What is the best possible cadence for small body science.** This not only includes deriving their rotation periods, but discovering new objects and improving the orbits of known objects.

- **Can an all sky survey detect the YORP effect [12, 56]?** YORP has been detected through targeted campaigns, but if a survey like LSST could detect it, the number of objects that have undergone YORP can be greatly increased.

- **Can a simulation of LSST be used to better constrain the perihelion gap problem [49] after LSST has observed new extreme TNOs.** A simulation of LSST can be done where the only objects are TNOs and it can be determined how efficient LSST is at detecting and confirming now TNOs in different parts of the sky.

- **What is the effect of an incorrect phase curve slope parameter (Appendix C) on the derivation of rotation period.** If a bad solution is used, the geometry of the observation might not be fully removed. I suspect this would only effect super slow rotation derivation as the timescale of the rotation and orbital period are similar.

- **Can GPULS [24] be improved for large datasets to compute some LSPs on the CPU?** A hybrid algorithm could increase performance since the CPU is idle while GPULS is running.

- **Can all sky surveys be used to calculate shape models for small bodies?** Modeling the shape of small bodies is a subject I have not discussed here, but, since LSST will observe so many objects, determining if it can derive the shapes is important.

- **Use several of the de-aliasing methods together to see if that improves the period match rate.** In Chapter 2, the methods were used independently of each other, but maybe some combination of them would improve the match percentage more than just one by itself.

Bibliography

[1] Charles Acton, Nathaniel Bachman, Boris Semenov, and Edward Wright. A look towards the future in the handling of space science mission geometry. *Planetary and Space Science*, 150:9–12, 2018. ISSN 0032-0633. doi: https://doi.org/10.1016/j.pss.2017.02.013. URL `https://www.sciencedirect.com/science/article/pii/S0032063316303129`. Enabling Open and Interoperable Access to Planetary Science and Heliophysics Databases and Tools.

[2] Charles H. Acton. Ancillary data services of nasa's navigation and ancillary information facility. *Planetary and Space Science*, 44(1):65–70, 1996. ISSN 0032-0633. doi: https://doi.org/10.1016/0032-0633(95)00107-7. URL `https://www.sciencedirect.com/science/article/pii/0032063395001077`. Planetary data system.

[3] Andrew M. Annex, Ben Pearson, Benoît Seignovert, Brian T. Carcich, Helge Eichhorn, Jesse A. Mapel, Johan L. Freiherr von Forstner, Jonathan McAuliffe, Jorge Diaz del Rio, Kristin L. Berry, K.-Michael Aye, Marcel Stefko, Miguel de Val-Borro, Shankar Kulumani, and Shin ya Murakami. Spiceypy: a pythonic wrapper for the spice toolkit. *Journal of Open Source Software*, 5(46):2050, 2020. doi: 10.21105/joss.02050. URL `https://doi.org/10.21105/joss.02050`.

[4] Astropy Collaboration, T. P. Robitaille, E. J. Tollerud, P. Greenfield, M. Droettboom, E. Bray, T. Aldcroft, M. Davis, A. Ginsburg, A. M. Price-Whelan, W. E. Kerzendorf, A. Conley, N. Crighton, K. Barbary, D. Muna, H. Ferguson, F. Grollier, M. M. Parikh, P. H. Nair, H. M. Unther, C. Deil, J. Woillez, S. Conseil, R. Kramer, J. E. H. Turner,

L. Singer, R. Fox, B. A. Weaver, V. Zabalza, Z. I. Edwards, K. Azalee Bostroem, D. J. Burke, A. R. Casey, S. M. Crawford, N. Dencheva, J. Ely, T. Jenness, K. Labrie, P. L. Lim, F. Pierfederici, A. Pontzen, A. Ptak, B. Refsdal, M. Servillat, and O. Streicher. Astropy: A community Python package for astronomy. *Astronomy and Astrophysics*, 558:A33, October 2013. doi: 10.1051/0004-6361/201322068.

[5] Astropy Collaboration, A. M. Price-Whelan, B. M. Sipőcz, H. M. Günther, P. L. Lim, S. M. Crawford, S. Conseil, D. L. Shupe, M. W. Craig, N. Dencheva, A. Ginsburg, J. T. Vand erPlas, L. D. Bradley, D. Pérez-Suárez, M. de Val-Borro, T. L. Aldcroft, K. L. Cruz, T. P. Robitaille, E. J. Tollerud, C. Ardelean, T. Babej, Y. P. Bach, M. Bachetti, A. V. Bakanov, S. P. Bamford, G. Barentsen, P. Barmby, A. Baumbach, K. L. Berry, F. Biscani, M. Boquien, K. A. Bostroem, L. G. Bouma, G. B. Brammer, E. M. Bray, H. Breytenbach, H. Buddelmeijer, D. J. Burke, G. Calderone, J. L. Cano Rodríguez, M. Cara, J. V. M. Cardoso, S. Cheedella, Y. Copin, L. Corrales, D. Crichton, D. D'Avella, C. Deil, É. Depagne, J. P. Dietrich, A. Donath, M. Droettboom, N. Earl, T. Erben, S. Fabbro, L. A. Ferreira, T. Finethy, R. T. Fox, L. H. Garrison, S. L. J. Gibbons, D. A. Goldstein, R. Gommers, J. P. Greco, P. Greenfield, A. M. Groener, F. Grollier, A. Hagen, P. Hirst, D. Homeier, A. J. Horton, G. Hosseinzadeh, L. Hu, J. S. Hunkeler, Ž. Ivezić, A. Jain, T. Jenness, G. Kanarek, S. Kendrew, N. S. Kern, W. E. Kerzendorf, A. Khvalko, J. King, D. Kirkby, A. M. Kulkarni, A. Kumar, A. Lee, D. Lenz, S. P. Littlefair, Z. Ma, D. M. Macleod, M. Mastropietro, C. McCully, S. Montagnac, B. M. Morris, M. Mueller, S. J. Mumford, D. Muna, N. A. Murphy, S. Nelson, G. H. Nguyen, J. P. Ninan, M. Nöthe, S. Ogaz, S. Oh, J. K. Parejko, N. Parley, S. Pascual, R. Patil, A. A. Patil, A. L. Plunkett, J. X. Prochaska, T. Rastogi, V. Reddy Janga, J. Sabater, P. Sakurikar, M. Seifert, L. E. Sherbert, H. Sherwood-Taylor, A. Y. Shih, J. Sick, M. T. Silbiger, S. Singanamalla, L. P. Singer, P. H. Sladen, K. A. Sooley, S. Sornarajah, O. Streicher, P. Teuben, S. W. Thomas, G. R. Tremblay, J. E. H. Turner, V. Terrón, M. H. van Kerkwijk, A. de la Vega, L. L. Watkins, B. A. Weaver, J. B. Whit-

more, J. Woillez, V. Zabalza, and Astropy Contributors. The Astropy Project: Building an Open-science Project and Status of the v2.0 Core Package. *Astronomical Journal*, 156(3):123, September 2018. doi: 10.3847/1538-3881/aabc4f.

[6] Astropy Collaboration, Adrian M. Price-Whelan, Pey Lian Lim, Nicholas Earl, Nathaniel Starkman, Larry Bradley, David L. Shupe, Aarya A. Patil, Lia Corrales, C. E. Brasseur, Maximilian N"othe, Axel Donath, Erik Tollerud, Brett M. Morris, Adam Ginsburg, Eero Vaher, Benjamin A. Weaver, James Tocknell, William Jamieson, Marten H. van Kerkwijk, Thomas P. Robitaille, Bruce Merry, Matteo Bachetti, H. Moritz G"unther, Thomas L. Aldcroft, Jaime A. Alvarado-Montes, Anne M. Archibald, Attila B'odi, Shreyas Bapat, Geert Barentsen, Juanjo Baz'an, Manish Biswas, M'ed'eric Boquien, D. J. Burke, Daria Cara, Mihai Cara, Kyle E. Conroy, Simon Conseil, Matthew W. Craig, Robert M. Cross, Kelle L. Cruz, Francesco D'Eugenio, Nadia Dencheva, Hadrien A. R. Devillepoix, J"org P. Dietrich, Arthur Davis Eigenbrot, Thomas Erben, Leonardo Ferreira, Daniel Foreman-Mackey, Ryan Fox, Nabil Freij, Suyog Garg, Robel Geda, Lauren Glattly, Yash Gondhalekar, Karl D. Gordon, David Grant, Perry Greenfield, Austen M. Groener, Steve Guest, Sebastian Gurovich, Rasmus Handberg, Akeem Hart, Zac Hatfield-Dodds, Derek Homeier, Griffin Hosseinzadeh, Tim Jenness, Craig K. Jones, Prajwel Joseph, J. Bryce Kalmbach, Emir Karamehmetoglu, Mikolaj Kaluszy'nski, Michael S. P. Kelley, Nicholas Kern, Wolfgang E. Kerzendorf, Eric W. Koch, Shankar Kulumani, Antony Lee, Chun Ly, Zhiyuan Ma, Conor MacBride, Jakob M. Maljaars, Demitri Muna, N. A. Murphy, Henrik Norman, Richard O'Steen, Kyle A. Oman, Camilla Pacifici, Sergio Pascual, J. Pascual-Granado, Rohit R. Patil, Gabriel I. Perren, Timothy E. Pickering, Tanuj Rastogi, Benjamin R. Roulston, Daniel F. Ryan, Eli S. Rykoff, Jose Sabater, Parikshit Sakurikar, Jes'us Salgado, Aniket Sanghi, Nicholas Saunders, Volodymyr Savchenko, Ludwig Schwardt, Michael Seifert-Eckert, Albert Y. Shih, Anany Shrey Jain, Gyanendra Shukla, Jonathan Sick, Chris Simpson, Sudheesh Singanamalla, Leo P. Singer, Jaladh Singhal, Manodeep Sinha,

Brigitta M. SipHocz, Lee R. Spitler, David Stansby, Ole Streicher, Jani Sumak, John D. Swinbank, Dan S. Taranu, Nikita Tewary, Grant R. Tremblay, Miguel de Val-Borro, Samuel J. Van Kooten, Zlatan Vasovi'c, Shresth Verma, Jos'e Vin'icius de Miranda Cardoso, Peter K. G. Williams, Tom J. Wilson, Benjamin Winkel, W. M. Wood-Vasey, Rui Xue, Peter Yoachim, Chen Zhang, Andrea Zonca, and Astropy Project Contributors. The Astropy Project: Sustaining and Growing a Community-oriented Open-source Project and the Latest Major Release (v5.0) of the Core Package. *apj*, 935(2):167, August 2022. doi: 10.3847/1538-4357/ac7c74.

[7] R. V. Baluev. Assessing the statistical significance of periodogram peaks. *Monthly Notices of the Royal Astronomical Society*, 385(3):1279–1285, April 2008. doi: 10.1111/j.1365-2966.2008.12689.x.

[8] Nicholas H. Barbara, Timothy R. Bedding, Ben D. Fulcher, Simon J. Murphy, and Timothy Van Reeth. Classifying Kepler light curves for 12,000 A and F stars using supervised feature-based machine learning. *Monthly Notices of the Royal Astronomical Society*, June 2022. doi: 10.1093/mnras/stac1515.

[9] A. C. Becker, J. J. Bochanski, S. L. Hawley, Ž. Ivezić, A. F. Kowalski, B. Sesar, and A. A. West. Periodic Variability of Low-mass Stars in Sloan Digital Sky Survey Stripe 82. *The Astrophysical Journal*, 731(1):17, April 2011. doi: 10.1088/0004-637X/731/1/17.

[10] Eric C. Bellm, Shrinivas R. Kulkarni, Matthew J. Graham, Richard Dekany, Roger M. Smith, Reed Riddle, Frank J. Masci, George Helou, Thomas A. Prince, Scott M. Adams, C. Barbarino, Tom Barlow, James Bauer, Ron Beck, Justin Belicki, Rahul Biswas, Nadejda Blagorodnova, Dennis Bodewits, Bryce Bolin, Valery Brinnel, Tim Brooke, Brian Bue, Mattia Bulla, Rick Burruss, S. Bradley Cenko, Chan-Kao Chang, Andrew Connolly, Michael Coughlin, John Cromer, Virginia Cunningham, Kishalay De, Alex Delacroix, Vandana Desai, Dmitry A. Duev, Gwendolyn Eadie, Tony L. Farnham, Michael Feeney, Ulrich Feindt, David Flynn, Anna Franckowiak, S. Frederick, C. Frem-

ling, Avishay Gal-Yam, Suvi Gezari, Matteo Giomi, Daniel A. Goldstein, V. Zach Golkhou, Ariel Goobar, Steven Groom, Eugean Hacopians, David Hale, John Henning, Anna Y. Q. Ho, David Hover, Justin Howell, Tiara Hung, Daniela Huppenkothen, David Imel, Wing-Huen Ip, Željko Ivezić, Edward Jackson, Lynne Jones, Mario Juric, Mansi M. Kasliwal, S. Kaspi, Stephen Kaye, Michael S. P. Kelley, Marek Kowalski, Emily Kramer, Thomas Kupfer, Walter Landry, Russ R. Laher, Chien-De Lee, Hsing Wen Lin, Zhong-Yi Lin, Ragnhild Lunnan, Matteo Giomi, Ashish Mahabal, Peter Mao, Adam A. Miller, Serge Monkewitz, Patrick Murphy, Chow-Choong Ngeow, Jakob Nordin, Peter Nugent, Eran Ofek, Maria T. Patterson, Bryan Penprase, Michael Porter, Ludwig Rauch, Umaa Rebbapragada, Dan Reiley, Mickael Rigault, Hector Rodriguez, Jan van Roestel, Ben Rusholme, Jakob van Santen, S. Schulze, David L. Shupe, Leo P. Singer, Maayane T. Soumagnac, Robert Stein, Jason Surace, Jesper Sollerman, Paula Szkody, F. Taddia, Scott Terek, Angela Van Sistine, Sjoert van Velzen, W. Thomas Vestrand, Richard Walters, Charlotte Ward, Quan-Zhi Ye, Po-Chieh Yu, Lin Yan, and Jeffry Zolkower. The Zwicky Transient Facility: System Overview, Performance, and First Results. *Publications of the Astronomical Society of the Pacific*, 131(995):018002, December 2018. ISSN 1538-3873. doi: 10.1088/1538-3873/aaecbe.

[11] W. F. Bottke, M. Brož, D. P. O'Brien, A. Campo Bagatin, A. Morbidelli, and S. Marchi. *The Collisional Evolution of the Main Asteroid Belt*. January 2015. doi: 10.2458/azu_uapress_9780816532131-ch036.

[12] William F. Bottke, David Vokrouhlický, David P. Rubincam, and David Nesvorný. THE YARKOVSKY AND YORP EFFECTS: Implications for Asteroid Dynamics. *Annual Review of Earth and Planetary Sciences*, 34(1):157–191, 2006. doi: 10.1146/annurev.earth.34.031405.125154.

[13] Edward Bowell, Bruce Hapke, Deborah Domingue, Kari Lumme, Jouni Peltoniemi, and Alan W. Harris. Application of photometric models to asteroids. In Richard P. Binzel,

Tom Gehrels, and Mildred Shapley Matthews, editors, *Asteroids II*, pages 524–556, January 1989.

[14] E. O. Brigham and R. E. Morrow. The fast Fourier transform. *IEEE Spectrum*, 4(12): 63–70, December 1967. ISSN 1939-9340. doi: 10.1109/MSPEC.1967.5217220.

[15] M. Carbonell, R. Oliver, and J. L. Ballester. Power spectra of gapped time series - A comparison of several methods. *Astronomy and Astrophysics*, 264(1):350–360, October 1992.

[16] D. Coppersmith. An approximate Fourier transform useful in quantum factoring, January 2002.

[17] Michael W. Coughlin, Kevin Burdge, Dmitry A. Duev, Michael L. Katz, Jan van Roestel, Andrew Drake, Matthew J. Graham, Lynne Hillenbrand, Ashish A. Mahabal, Frank J. Masci, Przemek Mróz, Thomas A. Prince, Yuhan Yao, Eric C. Bellm, Rick Burruss, Richard Dekany, Amruta Jaodand, David L. Kaplan, Thomas Kupfer, Russ R. Laher, Reed Riddle, Mickael Rigault, Hector Rodriguez, Ben Rusholme, and Jeffry Zolkower. The ZTF Source Classification Project: II. Periodicity and variability processing metrics. *Monthly Notices of the Royal Astronomical Society*, 505(2):2954–2965, June 2021. ISSN 0035-8711, 1365-2966. doi: 10.1093/mnras/stab1502.

[18] L. Denneau. The ATLAS All-Sky Survey. In P. R. Wozniak, M. J. Graham, A. A. Mahabal, and R. Seaman, editors, *The Third Hot-wiring the Transient Universe Workshop*, pages 65–65, January 2014.

[19] Dmitry A Duev, Ashish Mahabal, Frank J Masci, Matthew J Graham, Ben Rusholme, Richard Walters, Ishani Karmarkar, Sara Frederick, Mansi M Kasliwal, Umaa Rebbapragada, and Charlotte Ward. Real-bogus classification for the Zwicky Transient Facility using deep learning. *Monthly Notices of the Royal Astronomical Society*,

489(3):3582–3590, 08 2019. ISSN 0035-8711. doi: 10.1093/mnras/stz2357. URL https://doi.org/10.1093/mnras/stz2357.

[20] N Erasmus, D Kramer, A McNeill, D E Trilling, P Janse van Rensburg, G T van Belle, J L Tonry, L Denneau, A Heinze, and H J Weiland. Discovery of superslow rotating asteroids with atlas and ztf photometry. *Monthly Notices of the Royal Astronomical Society*, 506(3):3872–3881, Jul 2021. ISSN 1365-2966. doi: 10.1093/mnras/stab1888. URL http://dx.doi.org/10.1093/mnras/stab1888.

[21] Jerome H. Friedman. A VARIABLE SPAN SMOOTHER. October 1984.

[22] Gaia Collaboration, T. Prusti, J. H. J. de Bruijne, A. G. A. Brown, A. Vallenari, C. Babusiaux, C. A. L. Bailer-Jones, U. Bastian, M. Biermann, D. W. Evans, L. Eyer, F. Jansen, C. Jordi, S. A. Klioner, U. Lammers, L. Lindegren, X. Luri, F. Mignard, D. J. Milligan, C. Panem, V. Poinsignon, D. Pourbaix, S. Randich, G. Sarri, P. Sartoretti, H. I. Siddiqui, C. Soubiran, V. Valette, F. van Leeuwen, N. A. Walton, C. Aerts, F. Arenou, M. Cropper, R. Drimmel, E. Høg, D. Katz, M. G. Lattanzi, W. O'Mullane, E. K. Grebel, A. D. Holland, C. Huc, X. Passot, L. Bramante, C. Cacciari, J. Castañeda, L. Chaoul, N. Cheek, F. De Angeli, C. Fabricius, R. Guerra, J. Hernández, A. Jean-Antoine-Piccolo, E. Masana, R. Messineo, N. Mowlavi, K. Nienartowicz, D. Ordóñez-Blanco, P. Panuzzo, J. Portell, P. J. Richards, M. Riello, G. M. Seabroke, P. Tanga, F. Thévenin, J. Torra, S. G. Els, G. Gracia-Abril, G. Comoretto, M. Garcia-Reinaldos, T. Lock, E. Mercier, M. Altmann, R. Andrae, T. L. Astraatmadja, I. Bellas-Velidis, K. Benson, J. Berthier, R. Blomme, G. Busso, B. Carry, A. Cellino, G. Clementini, S. Cowell, O. Creevey, J. Cuypers, M. Davidson, J. De Ridder, A. de Torres, L. Delchambre, A. Dell'Oro, C. Ducourant, Y. Frémat, M. García-Torres, E. Gosset, J. L. Halbwachs, N. C. Hambly, D. L. Harrison, M. Hauser, D. Hestroffer, S. T. Hodgkin, H. E. Huckle, A. Hutton, G. Jasniewicz, S. Jordan, M. Kontizas, A. J. Korn, A. C. Lanzafame, M. Manteiga, A. Moitinho, K. Muinonen, J. Osinde, E. Pancino, T. Pauwels, J. M. Pe-

tit, A. Recio-Blanco, A. C. Robin, L. M. Sarro, C. Siopis, M. Smith, K. W. Smith, A. Sozzetti, W. Thuillot, W. van Reeven, Y. Viala, U. Abbas, A. Abreu Aramburu, S. Accart, J. J. Aguado, P. M. Allan, W. Allasia, G. Altavilla, M. A. Álvarez, J. Alves, R. I. Anderson, A. H. Andrei, E. Anglada Varela, E. Antiche, T. Antoja, S. Antón, B. Arcay, A. Atzei, L. Ayache, N. Bach, S. G. Baker, L. Balaguer-Núñez, C. Barache, C. Barata, A. Barbier, F. Barblan, M. Baroni, D. Barrado y Navascués, M. Barros, M. A. Barstow, U. Becciani, M. Bellazzini, G. Bellei, A. Bello García, V. Belokurov, P. Bendjoya, A. Berihuete, L. Bianchi, O. Bienaymé, F. Billebaud, N. Blagorodnova, S. Blanco-Cuaresma, T. Boch, A. Bombrun, R. Borrachero, S. Bouquillon, G. Bourda, H. Bouy, A. Bragaglia, M. A. Breddels, N. Brouillet, T. Brüsemeister, B. Bucciarelli, F. Budnik, P. Burgess, R. Burgon, A. Burlacu, D. Busonero, R. Buzzi, E. Caffau, J. Cambras, H. Campbell, R. Cancelliere, T. Cantat-Gaudin, T. Carlucci, J. M. Carrasco, M. Castellani, P. Charlot, J. Charnas, P. Charvet, F. Chassat, A. Chiavassa, M. Clotet, G. Cocozza, R. S. Collins, P. Collins, G. Costigan, F. Crifo, N. J. G. Cross, M. Crosta, C. Crowley, C. Dafonte, Y. Damerdji, A. Dapergolas, P. David, M. David, P. De Cat, F. de Felice, P. de Laverny, F. De Luise, R. De March, D. de Martino, R. de Souza, J. Debosscher, E. del Pozo, M. Delbo, A. Delgado, H. E. Delgado, F. di Marco, P. Di Matteo, S. Diakite, E. Distefano, C. Dolding, S. Dos Anjos, P. Drazinos, J. Durán, Y. Dzigan, E. Ecale, B. Edvardsson, H. Enke, M. Erdmann, D. Escolar, M. Espina, N. W. Evans, G. Eynard Bontemps, C. Fabre, M. Fabrizio, S. Faigler, A. J. Falcão, M. Farràs Casas, F. Faye, L. Federici, G. Fedorets, J. Fernández-Hernández, P. Fernique, A. Fienga, F. Figueras, F. Filippi, K. Findeisen, A. Fonti, M. Fouesneau, E. Fraile, M. Fraser, J. Fuchs, R. Furnell, M. Gai, S. Galleti, L. Galluccio, D. Garabato, F. García-Sedano, P. Garé, A. Garofalo, N. Garralda, P. Gavras, J. Gerssen, R. Geyer, G. Gilmore, S. Girona, G. Giuffrida, M. Gomes, A. González-Marcos, J. González-Núñez, J. J. González-Vidal, M. Granvik, A. Guerrier, P. Guillout, J. Guiraud, A. Gúrpide, R. Gutiérrez-Sánchez, L. P. Guy, R. Haigron, D. Hatzidim-

itriou, M. Haywood, U. Heiter, A. Helmi, D. Hobbs, W. Hofmann, B. Holl, G. Holland, J. A. S. Hunt, A. Hypki, V. Icardi, M. Irwin, G. Jevardat de Fombelle, P. Jofré, P. G. Jonker, A. Jorissen, F. Julbe, A. Karampelas, A. Kochoska, R. Kohley, K. Kolenberg, E. Kontizas, S. E. Koposov, G. Kordopatis, P. Koubsky, A. Kowalczyk, A. Krone-Martins, M. Kudryashova, I. Kull, R. K. Bachchan, F. Lacoste-Seris, A. F. Lanza, J. B. Lavigne, C. Le Poncin-Lafitte, Y. Lebreton, T. Lebzelter, S. Leccia, N. Leclerc, I. Lecoeur-Taibi, V. Lemaitre, H. Lenhardt, F. Leroux, S. Liao, E. Licata, H. E. P. Lindstrøm, T. A. Lister, E. Livanou, A. Lobel, W. Löffler, M. López, A. Lopez-Lozano, D. Lorenz, T. Loureiro, I. MacDonald, T. Magalhães Fernandes, S. Managau, R. G. Mann, G. Mantelet, O. Marchal, J. M. Marchant, M. Marconi, J. Marie, S. Marinoni, P. M. Marrese, G. Marschalkó, D. J. Marshall, J. M. Martín-Fleitas, M. Martino, N. Mary, G. Matijevič, T. Mazeh, P. J. McMillan, S. Messina, A. Mestre, D. Michalik, N. R. Millar, B. M. H. Miranda, D. Molina, R. Molinaro, M. Molinaro, L. Molnár, M. Moniez, P. Montegriffo, D. Monteiro, R. Mor, A. Mora, R. Morbidelli, T. Morel, S. Morgenthaler, T. Morley, D. Morris, A. F. Mulone, T. Muraveva, I. Musella, J. Narbonne, G. Nelemans, L. Nicastro, L. Noval, C. Ordénovic, J. Ordieres-Meré, P. Osborne, C. Pagani, I. Pagano, F. Pailler, H. Palacin, L. Palaversa, P. Parsons, T. Paulsen, M. Pecoraro, R. Pedrosa, H. Pentikäinen, J. Pereira, B. Pichon, A. M. Piersimoni, F. X. Pineau, E. Plachy, G. Plum, E. Poujoulet, A. Prša, L. Pulone, S. Ragaini, S. Rago, N. Rambaux, M. Ramos-Lerate, P. Ranalli, G. Rauw, A. Read, S. Regibo, F. Renk, C. Reylé, R. A. Ribeiro, L. Rimoldini, V. Ripepi, A. Riva, G. Rixon, M. Roelens, M. Romero-Gómez, N. Rowell, F. Royer, A. Rudolph, L. Ruiz-Dern, G. Sadowski, T. Sagristà Sellés, J. Sahlmann, J. Salgado, E. Salguero, M. Sarasso, H. Savietto, A. Schnorhk, M. Schultheis, E. Sciacca, M. Segol, J. C. Segovia, D. Segransan, E. Serpell, I. C. Shih, R. Smareglia, R. L. Smart, C. Smith, E. Solano, F. Solitro, R. Sordo, S. Soria Nieto, J. Souchay, A. Spagna, F. Spoto, U. Stampa, I. A. Steele, H. Steidelmüller, C. A. Stephenson, H. Stoev, F. F. Suess, M. Süveges, J. Surdej,

L. Szabados, E. Szegedi-Elek, D. Tapiador, F. Taris, G. Tauran, M. B. Taylor, R. Teixeira, D. Terrett, B. Tingley, S. C. Trager, C. Turon, A. Ulla, E. Utrilla, G. Valentini, A. van Elteren, E. Van Hemelryck, M. van Leeuwen, M. Varadi, A. Vecchiato, J. Veljanoski, T. Via, D. Vicente, S. Vogt, H. Voss, V. Votruba, S. Voutsinas, G. Walmsley, M. Weiler, K. Weingrill, D. Werner, T. Wevers, G. Whitehead, Ł. Wyrzykowski, A. Yoldas, M. Žerjal, S. Zucker, C. Zurbach, T. Zwitter, A. Alecu, M. Allen, C. Allende Prieto, A. Amorim, G. Anglada-Escudé, V. Arsenijevic, S. Azaz, P. Balm, M. Beck, H. H. Bernstein, L. Bigot, A. Bijaoui, C. Blasco, M. Bonfigli, G. Bono, S. Boudreault, A. Bressan, S. Brown, P. M. Brunet, P. Bunclark, R. Buonanno, A. G. Butkevich, C. Carret, C. Carrion, L. Chemin, F. Chéreau, L. Corcione, E. Darmigny, K. S. de Boer, P. de Teodoro, P. T. de Zeeuw, C. Delle Luche, C. D. Domingues, P. Dubath, F. Fodor, B. Frézouls, A. Fries, D. Fustes, D. Fyfe, E. Gallardo, J. Gallegos, D. Gardiol, M. Gebran, A. Gomboc, A. Gómez, E. Grux, A. Gueguen, A. Heyrovsky, J. Hoar, G. Iannicola, Y. Isasi Parache, A. M. Janotto, E. Joliet, A. Jonckheere, R. Keil, D. W. Kim, P. Klagyivik, J. Klar, J. Knude, O. Kochukhov, I. Kolka, J. Kos, A. Kutka, V. Lainey, D. LeBouquin, C. Liu, D. Loreggia, V. V. Makarov, M. G. Marseille, C. Martayan, O. Martinez-Rubi, B. Massart, F. Meynadier, S. Mignot, U. Munari, A. T. Nguyen, T. Nordlander, P. Ocvirk, K. S. O'Flaherty, A. Olias Sanz, P. Ortiz, J. Osorio, D. Oszkiewicz, A. Ouzounis, M. Palmer, P. Park, E. Pasquato, C. Peltzer, J. Peralta, F. Péturaud, T. Pieniluoma, E. Pigozzi, J. Poels, G. Prat, T. Prod'homme, F. Raison, J. M. Rebordao, D. Risquez, B. Rocca-Volmerange, S. Rosen, M. I. Ruiz-Fuertes, F. Russo, S. Sembay, I. Serraller Vizcaino, A. Short, A. Siebert, H. Silva, D. Sinachopoulos, E. Slezak, M. Soffel, D. Sosnowska, V. Straižys, M. ter Linden, D. Terrell, S. Theil, C. Tiede, L. Troisi, P. Tsalmantza, D. Tur, M. Vaccari, F. Vachier, P. Valles, W. Van Hamme, L. Veltz, J. Virtanen, J. M. Wallut, R. Wichmann, M. I. Wilkinson, H. Ziaeepour, and S. Zschocke. The Gaia mission. *Astronomy and Atrophysics*, 595:A1, November 2016. doi: 10.1051/0004-6361/201629272.

[23] M. Gowanlock, N. R. Butler, D. E. Trilling, and A. McNeill. GPU-enabled searches for periodic signals of unknown shape. *Astronomy and Computing*, 38:100511, January 2022. ISSN 2213-1337. doi: 10.1016/j.ascom.2021.100511.

[24] Michael Gowanlock, Daniel Kramer, David E. Trilling, Nathaniel R. Butler, and Brian Donnelly. Fast period searches using the lomb-scargle algorithm on graphics processing units for large datasets and real-time applications, 2021. URL `https://arxiv.org/abs/2105.04006`.

[25] Matthew J. Graham, Andrew J. Drake, S. G. Djorgovski, Ashish A. Mahabal, and Ciro Donalek. Using conditional entropy to identify periodicity. *Monthly Notices of the Royal Astronomical Society*, 434(3):2629–2635, September 2013. ISSN 0035-8711. doi: 10.1093/mnras/stt1206.

[26] M. Granvik, J. Virtanen, D. Oszkiewicz, and K. Muinonen. OpenOrb: Open-source asteroid orbit computation software including statistical ranging. *Meteoritics & Planetary Science*, 44(12):1853–1861, January 2009. doi: 10.1111/j.1945-5100.2009.tb01994.x.

[27] Tommy Grav, Robert Jedicke, Larry Denneau, Steve Chesley, Matthew J. Holman, and Timothy B. Spahr. The pan-starrs synthetic solar system model: A tool for testing and efficiency determination of the moving object processing system. *Publications of the Astronomical Society of the Pacific*, 123(902):423–447, 2011. ISSN 00046280, 15383873. URL `http://www.jstor.org/stable/10.1086/659833`.

[28] Charles R. Harris, K. Jarrod Millman, Stéfan J. van der Walt, Ralf Gommers, Pauli Virtanen, David Cournapeau, Eric Wieser, Julian Taylor, Sebastian Berg, Nathaniel J. Smith, Robert Kern, Matti Picus, Stephan Hoyer, Marten H. van Kerkwijk, Matthew Brett, Allan Haldane, Jaime Fernández del Río, Mark Wiebe, Pearu Peterson, Pierre Gérard-Marchant, Kevin Sheppard, Tyler Reddy, Warren Weckesser, Hameer Abbasi, Christoph Gohlke, and Travis E. Oliphant. Array programming with NumPy. *Nature*,

585(7825):357–362, September 2020. doi: 10.1038/s41586-020-2649-2. URL https://doi.org/10.1038/s41586-020-2649-2.

[29] A. N. Heinze, John L. Tonry, Larry Denneau, Heather Flewelling, Brian Stalder, Armin Rest, Ken W. Smith, Stephen J. Smartt, and Henry Weiland. A First Catalog of Variable Stars Measured by the Asteroid Terrestrial-impact Last Alert System (ATLAS). *The Astronomical Journal*, 156(5):241, November 2018. ISSN 1538-3881. doi: 10.3847/1538-3881/aae47f.

[30] M. E. Huber, S. Nikolaev, K. H. Cook, A. Rest, C. Smith, K. Olsen, N. Suntzeff, C. Aguilera, C. Stubbs, A. Garg, P. Challis, A. Becker, R. Covarrubias, A. Miceli, D. Welch, G. Miknaitis, J. L. Prieto, A. Clocchiatti, D. Minniti, and L. Morelli. Mining the Variables Out of the SuperMACHO Dataset. In *American Astronomical Society Meeting Abstracts*, volume 207 of *American Astronomical Society Meeting Abstracts*, page 122.16, December 2005.

[31] J. D. Hunter. Matplotlib: A 2d graphics environment. *Computing in Science & Engineering*, 9(3):90–95, 2007. doi: 10.1109/mcse.2007.55.

[32] Ž. Ivezić, S. M. Kahn, J. A. Tyson, B. Abel, E. Acosta, R. Allsman, D. Alonso, Y. AlSayyad, S. F. Anderson, J. Andrew, and et al. LSST: From Science Drivers to Reference Design and Anticipated Data Products. *Astrophysical Journal*, 873:111, March 2019. doi: 10.3847/1538-4357/ab042c.

[33] R. Lynne Jones, Peter Yoachim, Srinivasan Chandrasekharan, Andrew J. Connolly, Kem H. Cook, Željko Ivezic, K. Simon Krughoff, Catherine Petry, and Stephen T. Ridgway. The LSST metrics analysis framework (MAF). In *Observatory Operations: Strategies, Processes, and Systems V*, volume 9149, pages 118–135. Spie, July 2014. doi: 10.1117/12.2056835.

[34] Mario Juric, Siegfried Eggl, Lynne Jones, Joachim Moeyens, Eric Bellm, Zeljko Ivezic,

Nate Lust, Steven Stetzler, Samuel Cornwall, Aidan Berres, Maria Chernyavskaya, and Rubin Observatory Construction Project. Being Ready at First Light: 10yr Simulations of the Legacy Survey of Space and Time (LSST). *Bulletin of the AAS*, 53(7), oct 3 2021. https://baas.aas.org/pub/2021n7i101p06.

[35] Scott Kenyon, Benjamin Bromley, David O'Brien, and Don Davis. Formation and collisional evolution of kuiper belt objects. *The Solar System beyond Neptune*, 05 2007.

[36] D. Kramer, M. Gowanlock, D. Trilling, A. McNeill, and N. Erasmus. Removing aliases in time-series photometry. *Astronomy and Computing*, page 100711, 2023. ISSN 2213-1337. doi: https://doi.org/10.1016/j.ascom.2023.100711. URL `https://www.sciencedirect.com/science/article/pii/S2213133723000264`.

[37] Daniel Kramer, Michael Gowanlock, and Trilling David. The Effect of Different LSST Cadences on Derived Rotation Periods for Solar System Small Bodies. *Submitted*, 2023.

[38] N. R. Lomb. Least-Squares Frequency Analysis of Unequally Spaced Data. *Astrophysics and Space Science*, 39(2):447–462, February 1976. doi: 10.1007/BF00648343.

[39] LSST Science Collaboration, Paul A. Abell, Julius Allison, Scott F. Anderson, John R. Andrew, J. Roger P. Angel, Lee Armus, David Arnett, S. J. Asztalos, Tim S. Axelrod, Stephen Bailey, D. R. Ballantyne, Justin R. Bankert, Wayne A. Barkhouse, Jeffrey D. Barr, L. Felipe Barrientos, Aaron J. Barth, James G. Bartlett, Andrew C. Becker, Jacek Becla, Timothy C. Beers, Joseph P. Bernstein, Rahul Biswas, Michael R. Blanton, Joshua S. Bloom, John J. Bochanski, Pat Boeshaar, Kirk D. Borne, Marusa Bradac, W. N. Brandt, Carrie R. Bridge, Michael E. Brown, Robert J. Brunner, James S. Bullock, Adam J. Burgasser, James H. Burge, David L. Burke, Phillip A. Cargile, Srinivasan Chandrasekharan, George Chartas, Steven R. Chesley, You-Hua Chu, David Cinabro, Mark W. Claire, Charles F. Claver, Douglas Clowe, A. J. Connolly, Kem H. Cook, Jeff Cooke, Asantha Cooray, Kevin R. Covey, Christopher S. Culliton, Roelof de

Jong, Willem H. de Vries, Victor P. Debattista, Francisco Delgado, Ian P. Dell'Antonio, Saurav Dhital, Rosanne Di Stefano, Mark Dickinson, Benjamin Dilday, S. G. Djorgovski, Gregory Dobler, Ciro Donalek, Gregory Dubois-Felsmann, Josef Durech, Ardis Eliasdottir, Michael Eracleous, Laurent Eyer, Emilio E. Falco, Xiaohui Fan, Christopher D. Fassnacht, Harry C. Ferguson, Yanga R. Fernandez, Brian D. Fields, Douglas Finkbeiner, Eduardo E. Figueroa, Derek B. Fox, Harold Francke, James S. Frank, Josh Frieman, Sebastien Fromenteau, Muhammad Furqan, Gaspar Galaz, A. Gal-Yam, Peter Garnavich, Eric Gawiser, John Geary, Perry Gee, Robert R. Gibson, Kirk Gilmore, Emily A. Grace, Richard F. Green, William J. Gressler, Carl J. Grillmair, Salman Habib, J. S. Haggerty, Mario Hamuy, Alan W. Harris, Suzanne L. Hawley, Alan F. Heavens, Leslie Hebb, Todd J. Henry, Edward Hileman, Eric J. Hilton, Keri Hoadley, J. B. Holberg, Matt J. Holman, Steve B. Howell, Leopoldo Infante, Zeljko Ivezic, Suzanne H. Jacoby, Bhuvnesh Jain, R, Jedicke, M. James Jee, J. Garrett Jernigan, Saurabh W. Jha, Kathryn V. Johnston, R. Lynne Jones, Mario Juric, Mikko Kaasalainen, Styliani, Kafka, Steven M. Kahn, Nathan A. Kaib, Jason Kalirai, Jeff Kantor, Mansi M. Kasliwal, Charles R. Keeton, Richard Kessler, Zoran Knezevic, Adam Kowalski, Victor L. Krabbendam, K. Simon Krughoff, Shrinivas Kulkarni, Stephen Kuhlman, Mark Lacy, Sebastien Lepine, Ming Liang, Amy Lien, Paulina Lira, Knox S. Long, Suzanne Lorenz, Jennifer M. Lotz, R. H. Lupton, Julie Lutz, Lucas M. Macri, Ashish A. Mahabal, Rachel Mandelbaum, Phil Marshall, Morgan May, Peregrine M. McGehee, Brian T. Meadows, Alan Meert, Andrea Milani, Christopher J. Miller, Michelle Miller, David Mills, Dante Minniti, David Monet, Anjum S. Mukadam, Ehud Nakar, Douglas R. Neill, Jeffrey A. Newman, Sergei Nikolaev, Martin Nordby, Paul O'Connor, Masamune Oguri, John Oliver, Scot S. Olivier, Julia K. Olsen, Knut Olsen, Edward W. Olszewski, Hakeem Oluseyi, Nelson D. Padilla, Alex Parker, Joshua Pepper, John R. Peterson, Catherine Petry, Philip A. Pinto, James L. Pizagno, Bogdan Popescu, Andrej Prsa, Veljko Radcka, M. Jordan Raddick, Andrew Rasmussen, Arne Rau, Jeonghee Rho, James E. Rhoads,

Gordon T. Richards, Stephen T. Ridgway, Brant E. Robertson, Rok Roskar, Abhijit Saha, Ata Sarajedini, Evan Scannapieco, Terry Schalk, Rafe Schindler, Samuel Schmidt, Sarah Schmidt, Donald P. Schneider, German Schumacher, Ryan Scranton, Jacques Sebag, Lynn G. Seppala, Ohad Shemmer, Joshua D. Simon, M. Sivertz, Howard A. Smith, J. Allyn Smith, Nathan Smith, Anna H. Spitz, Adam Stanford, Keivan G. Stassun, Jay Strader, Michael A. Strauss, Christopher W. Stubbs, Donald W. Sweeney, Alex Szalay, Paula Szkody, Masahiro Takada, Paul Thorman, David E. Trilling, Virginia Trimble, Anthony Tyson, Richard Van Berg, Daniel Vanden Berk, Jake VanderPlas, Licia Verde, Bojan Vrsnak, Lucianne M. Walkowicz, Benjamin D. Wandelt, Sheng Wang, Yun Wang, Michael Warner, Risa H. Wechsler, Andrew A. West, Oliver Wiecha, Benjamin F. Williams, Beth Willman, David Wittman, Sidney C. Wolff, W. Michael Wood-Vasey, Przemek Wozniak, Patrick Young, Andrew Zentner, and Hu Zhan. LSST Science Book, Version 2.0. *arXiv e-prints*, art. arXiv:0912.0201, December 2009.

[40] LSST Science Collaboration, Phil Marshall, Timo Anguita, Federica B. Bianco, Eric C. Bellm, Niel Brandt, Will Clarkson, Andy Connolly, Eric Gawiser, Zeljko Ivezic, Lynne Jones, Michelle Lochner, Michael B. Lund, Ashish Mahabal, David Nidever, Knut Olsen, Stephen Ridgway, Jason Rhodes, Ohad Shemmer, David Trilling, Kathy Vivas, Lucianne Walkowicz, Beth Willman, Peter Yoachim, Scott Anderson, Pierre Antilogus, Ruth Angus, Iair Arcavi, Humna Awan, Rahul Biswas, Keaton J. Bell, David Bennett, Chris Britt, Derek Buzasi, Dana I. Casetti-Dinescu, Laura Chomiuk, Chuck Claver, Kem Cook, James Davenport, Victor Debattista, Seth Digel, Zoheyr Doctor, R. E. Firth, Ryan Foley, Wen-fai Fong, Lluis Galbany, Mark Giampapa, John E. Gizis, Melissa L. Graham, Carl Grillmair, Phillipe Gris, Zoltan Haiman, Patrick Hartigan, Suzanne Hawley, Renee Hlozek, Saurabh W. Jha, C. Johns-Krull, Shashi Kanbur, Vassiliki Kalogera, Vinay Kashyap, Vishal Kasliwal, Richard Kessler, Alex Kim, Peter Kurczynski, Ofer Lahav, Michael C. Liu, Alex Malz, Raffaella Margutti, Tom Matheson, Jason D. McEwen, Peregrine McGehee, Soren Meibom, Josh Meyers, Dave Monet, Eric Neilsen, Jeffrey

Newman, Matt O'Dowd, Hiranya V. Peiris, Matthew T. Penny, Christina Peters, Radoslaw Poleski, Kara Ponder, Gordon Richards, Jeonghee Rho, David Rubin, Samuel Schmidt, Robert L. Schuhmann, Avi Shporer, Colin Slater, Nathan Smith, Marcelles Soares-Santos, Keivan Stassun, Jay Strader, Michael Strauss, Rachel Street, Christopher Stubbs, Mark Sullivan, Paula Szkody, Virginia Trimble, Tony Tyson, Miguel de Val-Borro, Stefano Valenti, Robert Wagoner, W. Michael Wood-Vasey, and Bevin Ashley Zauderer. Science-Driven Optimization of the LSST Observing Strategy, August 2017.

[41] Xiao-Ping Lu and David Jewitt. Dependence of Light Curves on Phase Angle and Asteroid Shape. *The Astronomical Journal*, 158(6):220, November 2019. ISSN 1538-3881. doi: 10.3847/1538-3881/ab4ce4.

[42] Bruce Margony. The sloan digital sky survey. *Philosophical Transactions of the Royal Society of London. Series A: Mathematical, Physical and Engineering Sciences*, 357 (1750):93–103, jan 1999. doi: 10.1098/rsta.1999.0316. URL `https://doi.org/10.1098%2Frsta.1999.0316`.

[43] J. R. Masiero, F. E. DeMeo, T. Kasuga, and A. H. Parker. Asteroid family physical properties. In *Asteroids IV*. University of Arizona Press, 2015. doi: 10.2458/azu_uapress_9780816532131-ch017. URL `https://doi.org/10.2458%2Fazu_uapress_9780816532131-ch017`.

[44] Andrew McNeill, David E. Trilling, and Michael Mommert. Constraints on the Density and Internal Strength of 1I/'Oumuamua. *Astrophysical Journal, Letters*, 857(1):L1, April 2018. doi: 10.3847/2041-8213/aab9ab.

[45] Minor Planet Center. The international astronomical union minor planet center. URL `https://minorplanetcenter.net/`.

[46] Michael Mommert, Michael S. p. Kelley, Miguel de Val-Borro, Jian-Yang Li, Gian-

nina Guzman, Brigitta Sipőcz, Josef Ďurech, Mikael Granvik, Will Grundy, Nick Moskovitz, Antti Penttilä, and Nalin Samarasinha. sbpy: A python module for small-body planetary astronomy. *Journal of Open Source Software*, 4(38):1426, 2019. doi: 10.21105/joss.01426. URL https://doi.org/10.21105/joss.01426.

[47] Karri Muinonen, Irina N. Belskaya, Alberto Cellino, Marco Delbò, Anny-Chantal Levasseur-Regourd, Antti Penttilä, and Edward F. Tedesco. A three-parameter magnitude phase function for asteroids. *Icarus*, 209(2):542–555, October 2010. doi: 10.1016/j.icarus.2010.04.003.

[48] Karri Muinonen, Irina N. Belskaya, Alberto Cellino, Marco Delbò, Anny-Chantal Levasseur-Regourd, Antti Penttilä, and Edward F. Tedesco. A three-parameter magnitude phase function for asteroids. *Icarus*, 209(2):542–555, 2010. ISSN 0019-1035. doi: https://doi.org/10.1016/j.icarus.2010.04.003. URL https://www.sciencedirect.com/science/article/pii/S001910351000151X.

[49] William J. Oldroyd and Chadwick A. Trujillo. Outer Solar System Perihelion Gap Formation through Interactions with a Hypothetical Distant Giant Planet. *The Astronomical Journal*, 162(2):39, August 2021. doi: 10.3847/1538-3881/abfb6f.

[50] The pandas development team. pandas-dev/pandas: Pandas, February 2020. URL https://doi.org/10.5281/zenodo.3509134.

[51] A. Penttilä, V. G. Shevchenko, O. Wilkman, and K. Muinonen. H, G_1, G_2 photometric phase function extended to low-accuracy data. *Planetary and Space Science*, 123:117–125, April 2016. doi: 10.1016/j.pss.2015.08.010.

[52] M. J. D. Powell. An efficient method for finding the minimum of a function of several variables without calculating derivatives. *The Computer Journal*, 7(2):155–162, 01 1964. ISSN 0010-4620. doi: 10.1093/comjnl/7.2.155. URL https://doi.org/10.1093/comjnl/7.2.155.

[53] RAPIDS Development Team. *RAPIDS: Collection of Libraries for End to End GPU Data Science*, 2018. URL `https://rapids.ai`.

[54] George R. Ricker, Joshua N. Winn, Roland Vanderspek, David W. Latham, Gá spár Á. Bakos, Jacob L. Bean, Zachory K. Berta-Thompson, Timothy M. Brown, Lars Buchhave, Nathaniel R. Butler, R. Paul Butler, William J. Chaplin, David Charbonneau, Jørgen Christensen-Dalsgaard, Mark Clampin, Drake Deming, John Doty, Nathan De Lee, Courtney Dressing, Edward W. Dunham, Michael Endl, Francois Fressin, Jian Ge, Thomas Henning, Matthew J. Holman, Andrew W. Howard, Shigeru Ida, Jon M. Jenkins, Garrett Jernigan, John Asher Johnson, Lisa Kaltenegger, Nobuyuki Kawai, Hans Kjeldsen, Gregory Laughlin, Alan M. Levine, Douglas Lin, Jack J. Lissauer, Phillip MacQueen, Geoffrey Marcy, Peter R. McCullough, Timothy D. Morton, Norio Narita, Martin Paegert, Enric Palle, Francesco Pepe, Joshua Pepper, Andreas Quirrenbach, Stephen A. Rinehart, Dimitar Sasselov, Bun'ei Sato, Sara Seager, Alessandro Sozzetti, Keivan G. Stassun, Peter Sullivan, Andrew Szentgyorgyi, Guillermo Torres, Stephane Udry, and Joel Villasenor. Transiting exoplanet survey satellite. *Journal of Astronomical Telescopes, Instruments, and Systems*, 1(1):014003, oct 2014. doi: 10.1117/1.jatis.1.1.014003. URL `https://doi.org/10.1117%2F1.jatis.1.1.014003`.

[55] D. H. Roberts, J. Lehar, and J. W. Dreher. Time series analysis with CLEAN. I. Derivation of a spectrum. *Astronomical Journal*, 93:968–989, April 1987. doi: 10.1086/114383.

[56] David Parry Rubincam. Radiative Spin-up and Spin-down of Small Asteroids. *Icarus*, 148(1):2–11, November 2000. ISSN 0019-1035. doi: 10.1006/icar.2000.6485.

[57] J. D. Scargle. Studies in astronomical time series analysis. II. Statistical aspects of spectral analysis of unevenly spaced data. *Astrophysical Journal*, 263:835–853, December 1982. doi: 10.1086/160554.

[58] C.E. Shannon. Communication in the presence of noise. *Proceedings of the IRE*, 37(1): 10–21, jan 1949. doi: 10.1109/jrproc.1949.232969. URL https://doi.org/10.1109/jrproc.1949.232969.

[59] M. F. Skrutskie, R. M. Cutri, R. Stiening, M. D. Weinberg, S. Schneider, J. M. Carpenter, C. Beichman, R. Capps, T. Chester, J. Elias, J. Huchra, J. Liebert, C. Lonsdale, D. G. Monet, S. Price, P. Seitzer, T. Jarrett, J. D. Kirkpatrick, J. E. Gizis, E. Howard, T. Evans, J. Fowler, L. Fullmer, R. Hurt, R. Light, E. L. Kopan, K. A. Marsh, H. L. McCallon, R. Tam, S. Van Dyk, and S. Wheelock. The Two Micron All Sky Survey (2MASS). *Astronomical Journal*, 131(2):1163–1183, February 2006. doi: 10.1086/498708.

[60] Gilbert Strang. Wavelets. *American Scientist*, 82(3):250–255, 1994. ISSN 00030996.

[61] David Trilling. in prep.

[62] David E. Trilling, Michael Gowanlock, Daniel Kramer, Andrew McNeill, Brian Donnelly, Nat Butler, and John Kececioglu. The solar system notification alert processing system (SNAPS): Design, architecture, and first data release (SNAPShot1). *The Astronomical Journal*, 165(3):111, feb 2023. doi: 10.3847/1538-3881/acac7f. URL https://doi.org/10.3847%2F1538-3881%2Facac7f.

[63] Jacob T. VanderPlas. Understanding the lomb–scargle periodogram. *The Astrophysical Journal Supplement Series*, 236(1):16, May 2018. ISSN 1538-4365. doi: 10.3847/1538-4365/aab766. URL http://dx.doi.org/10.3847/1538-4365/aab766.

[64] Josef Ďurech, Michael Vávra, Radim Vančo, and Nicolas Erasmus. Rotation Periods of Asteroids Determined With Bootstrap Convex Inversion From ATLAS Photometry. *Frontiers in Astronomy and Space Sciences*, 9:809771, February 2022. doi: 10.3389/fspas.2022.809771.

[65] Peter Vereš, Robert Jedicke, Alan Fitzsimmons, Larry Denneau, Mikael Granvik, Bryce Bolin, Serge Chastel, Richard J. Wainscoat, William S. Burgett, Kenneth C. Chambers, Heather Flewelling, Nick Kaiser, Eugen A. Magnier, Jeff S. Morgan, Paul A. Price, John L. Tonry, and Christopher Waters. Absolute magnitudes and slope parameters for 250,000 asteroids observed by Pan-STARRS PS1 - Preliminary results. *Icarus*, 261: 34–47, November 2015. doi: 10.1016/j.icarus.2015.08.007.

[66] Pauli Virtanen, Ralf Gommers, Travis E. Oliphant, Matt Haberland, Tyler Reddy, David Cournapeau, Evgeni Burovski, Pearu Peterson, Warren Weckesser, Jonathan Bright, Stéfan J. van der Walt, Matthew Brett, Joshua Wilson, K. Jarrod Millman, Nikolay Mayorov, Andrew R. J. Nelson, Eric Jones, Robert Kern, Eric Larson, C J Carey, İlhan Polat, Yu Feng, Eric W. Moore, Jake VanderPlas, Denis Laxalde, Josef Perktold, Robert Cimrman, Ian Henriksen, E. A. Quintero, Charles R. Harris, Anne M. Archibald, Antônio H. Ribeiro, Fabian Pedregosa, Paul van Mulbregt, and SciPy 1.0 Contributors. SciPy 1.0: Fundamental Algorithms for Scientific Computing in Python. *Nature Methods*, 17:261–272, 2020. doi: 10.1038/s41592-019-0686-2.

[67] Brian D. Warner, Alan W. Harris, and Petr Pravec. Asteroid lightcurve database (lcdb) bundle v4.0, 2021. URL `https://sbn.psi.edu/pds/resource/doi/lcdb_4.0.html`.

[68] Brian D. Warner, Alan W. Harris, and Petr Pravec. Asteroid Lightcurve Database (LCDB) Bundle V4.0, 2021.

[69] Wes McKinney. Data Structures for Statistical Computing in Python. In Stéfan van der Walt and Jarrod Millman, editors, *Proceedings of the 9th Python in Science Conference*, pages 56–61, 2010. doi: 10.25080/Majora-92bf1922-00a.

[70] Bang Wong. Points of view: Color blindness. *Nature Methods*, 8(6):441–441, June 2011. ISSN 1548-7105. doi: 10.1038/nmeth.1618.

Appendix A

De-Aliasing Appendix

A.1 LSST Generation

For each object from the LSST Synthetic Moving Objects Database, the following cuts/steps were taken in generating a periodic signal in their data

1. Import all objects with at least 30 observations in at least two filters.

2. Convert the apparent magnitudes to absolute magnitudes using the "filterg12" value as that filter's G. LSST uses the Bowell HG system [13] not the HG12 system [47] even though the field is called "filterg12". If that filter's "g12" data was NaN, then the average of the rest of the filter "g12" values were used. If all the filter's "g12" values are NaN, then a value of $G = 0.15$ was used for all filters.

3. A period and amplitude were generated for each object and a sine wave with those properties was added to the objects derived absolute magnitudes. Both were generated using the parameters located in Table A.1 and the resulting distributions are shown in Figure A.1. The truncated normal distribution used SciPy's `truncnorm` function and the gamma distribution used SciPy's `gamma` function.

4. For each filter, the mean of the absolute magnitudes, μ_H, was calculated. $H - \mu_H$ for each filter was then concatenated, resulting in a single band of data with $\mu_H = 0$.

5. The observation data along with the assigned period and amplitude values were stored.

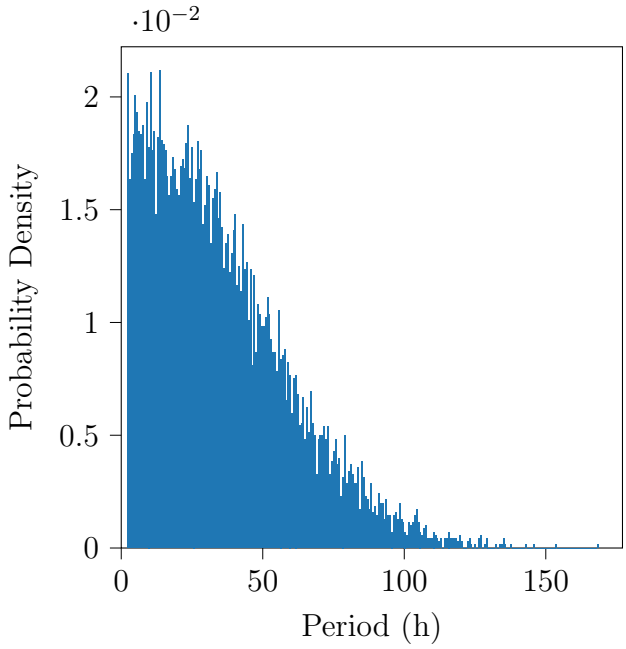

(a) The period distribution used for LSST.

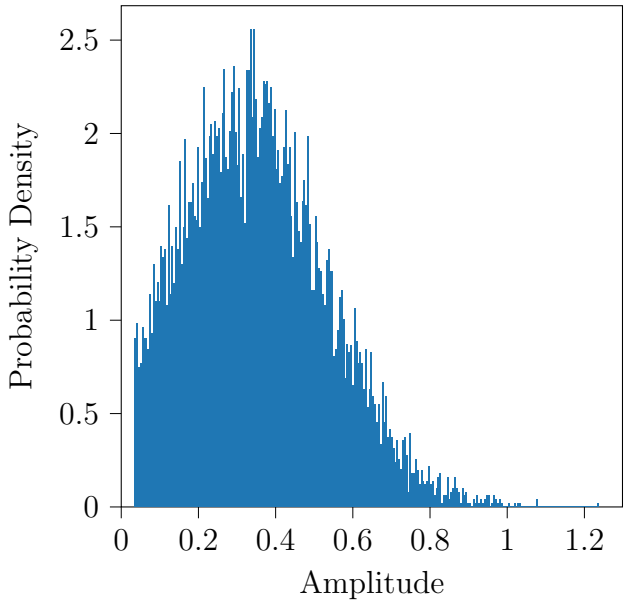

(b) The amplitude distribution used for LSST.

Figure A.1: The period and amplitude distributions for LSST. The x-axis is the period/amplitude and the y–axis is the probability density of each bin (the area under the histogram is 1).

	Period		Amplitude	
Distribution	Truncated Normal		Gamma	
Parameters	a	-0.1	a	0.48
	b	50	$\frac{1}{\beta}$	0.18
	μ	6		
	σ	40		

Table A.1: The distributions and parameters used for the period and amplitude generation. Plots for these distributions are available in Figure A.1. The distributions were approximated from the LCDB data (Section 2.4.1).

A.2 Derived Period Distributions

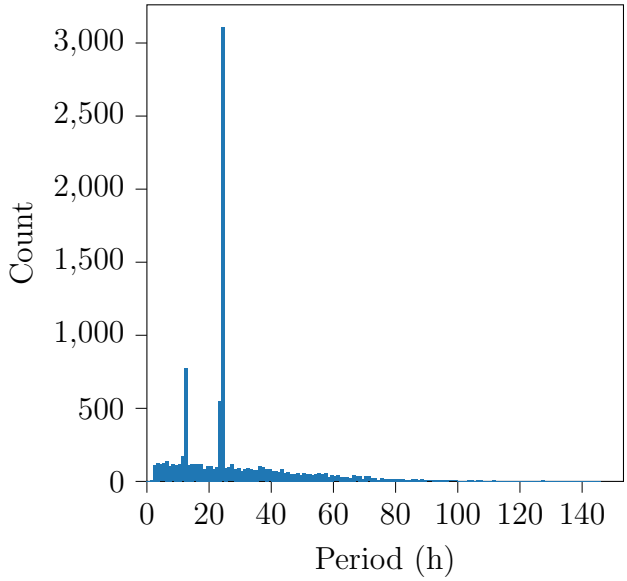

(a) LSST

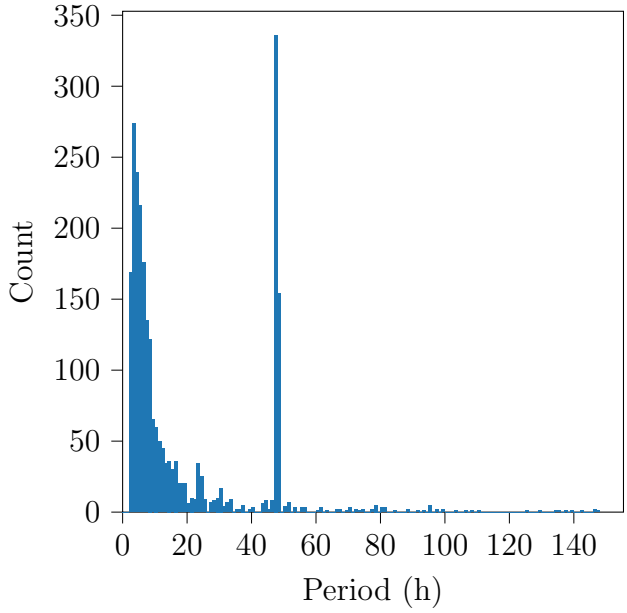

(b) ZTF

Figure A.2: The derived period distribution for the given survey using the no method (the base derived period distribution).

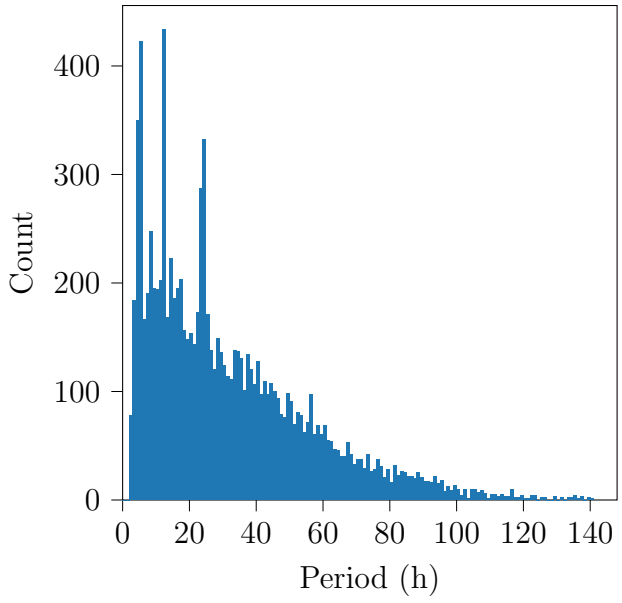

(a) LSST

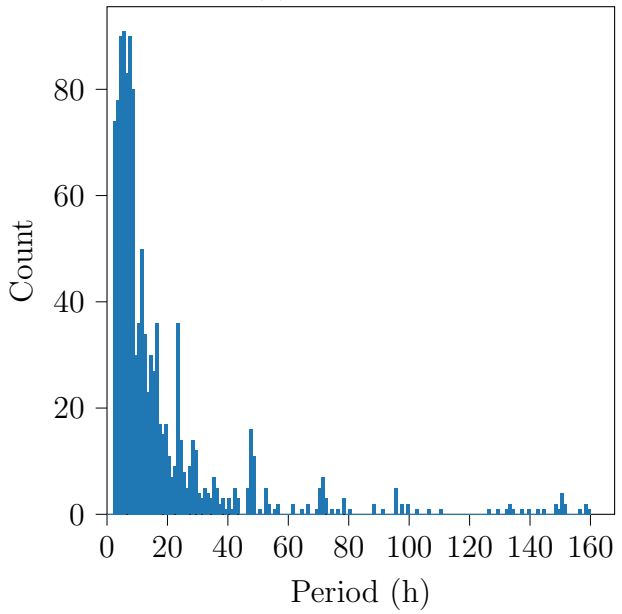

(b) ZTF

Figure A.3: The derived period distribution for the given survey using the mask method.

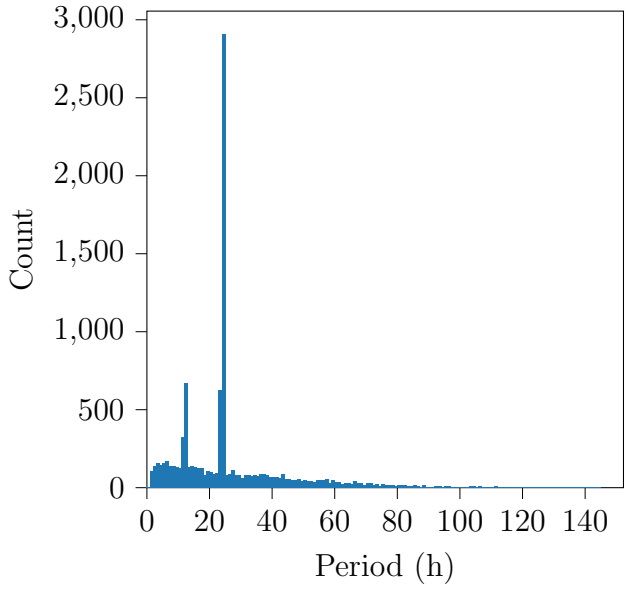

(a) LSST

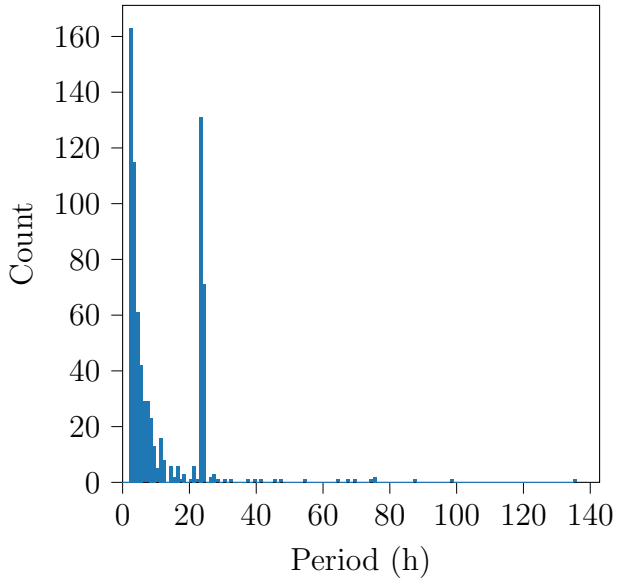

(b) ZTF

Figure A.4: The derived period distribution for the given survey using the MC method.

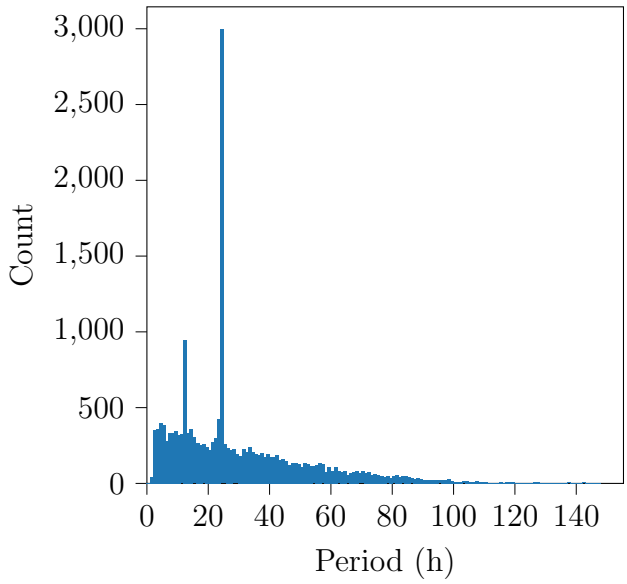

(a) LSST

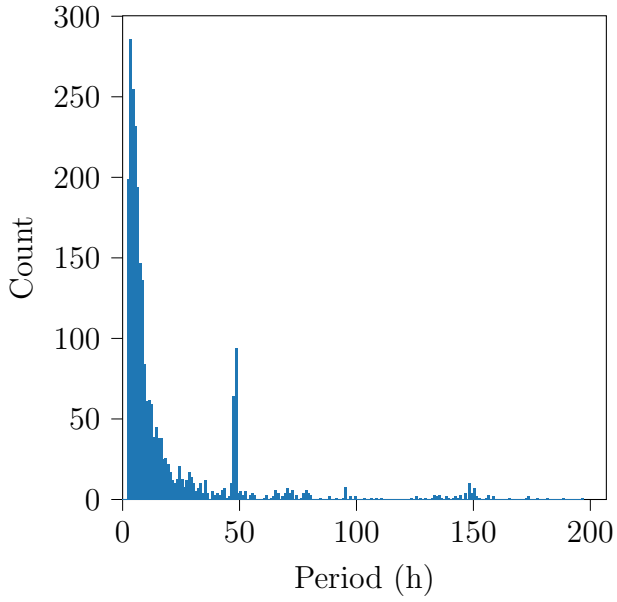

(b) ZTF

Figure A.5: The derived period distribution for the given survey using the window method.

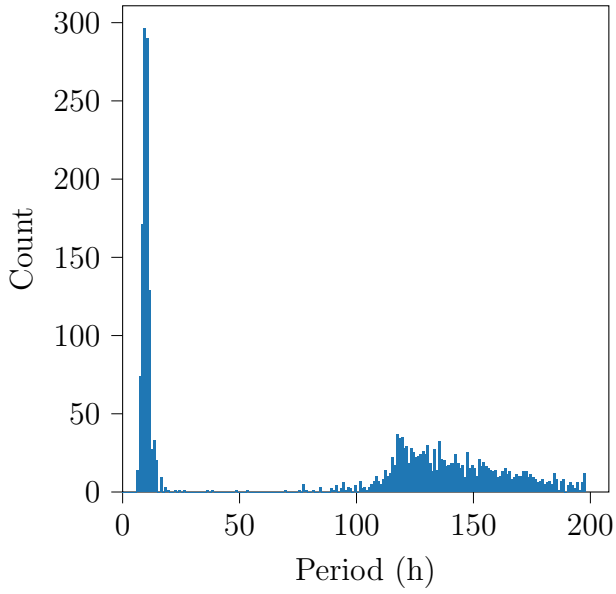

(a) LSST

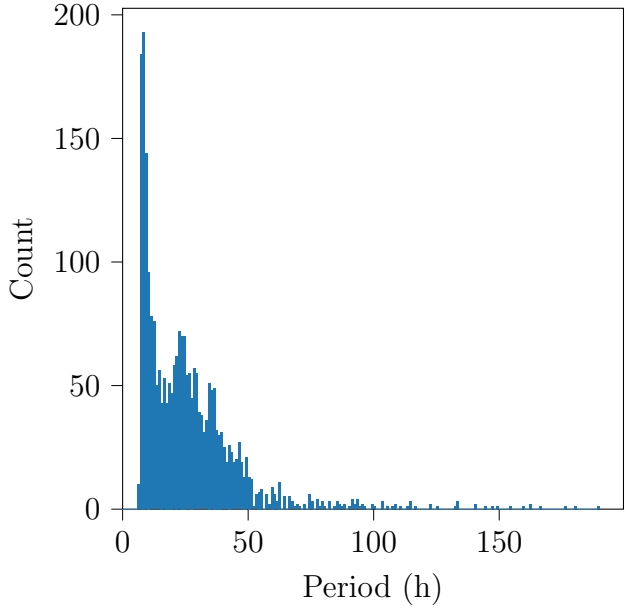

(b) ZTF

Figure A.6: The derived period distribution for the given survey using the VP method.

A.2.1 LSST Period Distributions Over Time

Figure A.7 shows the derived rotation period distribution for every year of LSST with no de-aliasing. The main difference each year is the growth of the 24 h alias. In years 1 to 3, the alias peak is not that extreme, but past year 4, the peak becomes more prominent.

Table 2.1 and Figure 2.2 shows that there are more aliases than just the 24 h and 48 h aliases shown in Figure A.7 (remember that Table 2.1 and Figure 2.2 are light-curve periods while Figure A.7 are rotation periods). Those peaks are not reflected in the figure because the other aliases are "weaker" and only appear once the "stronger" aliases are removed.

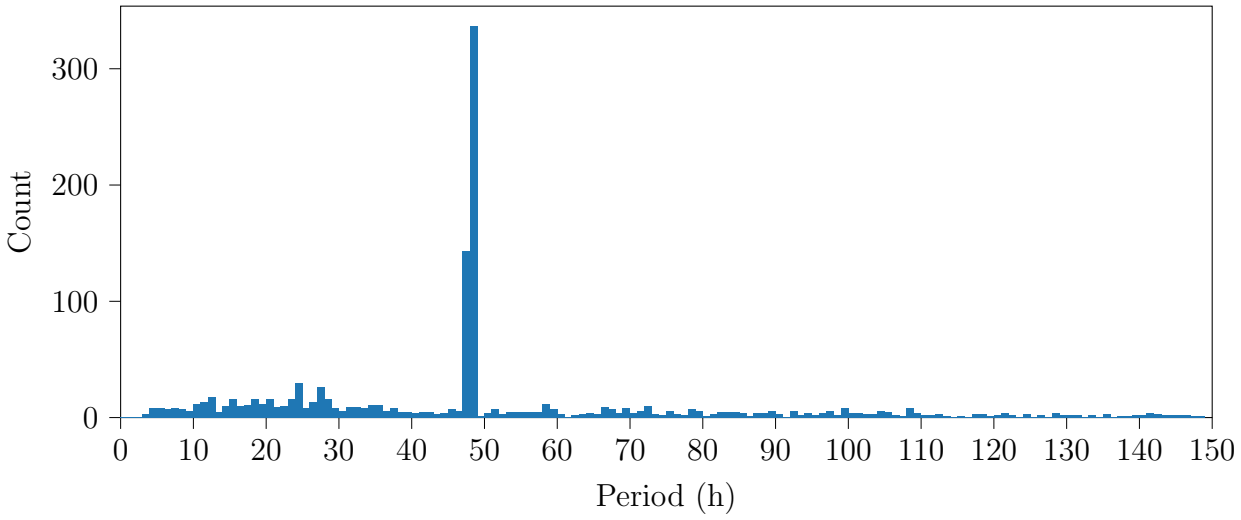

(a) Year 1

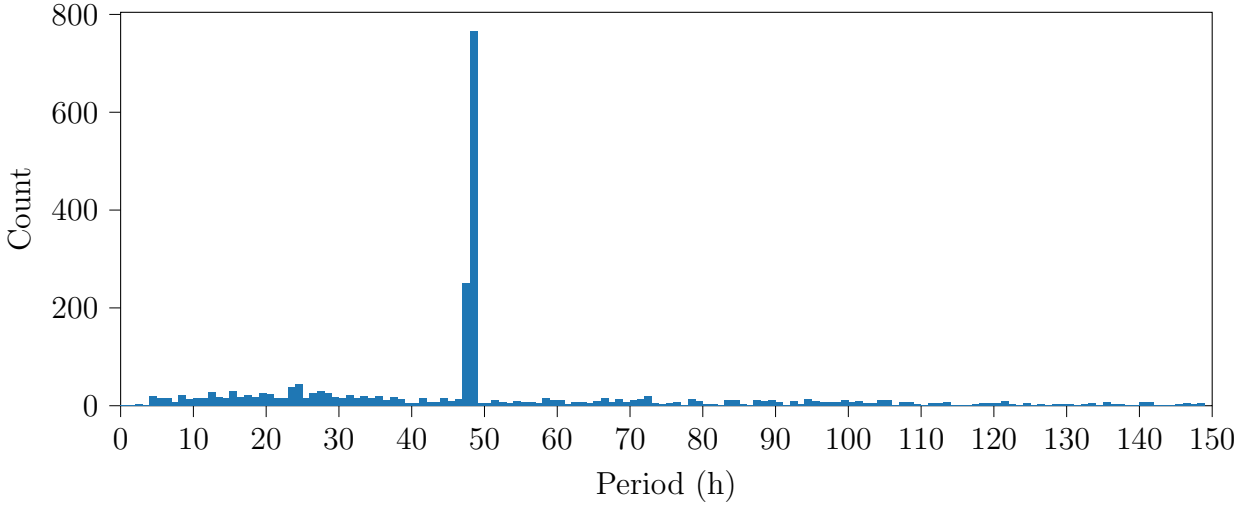

(b) Year 2

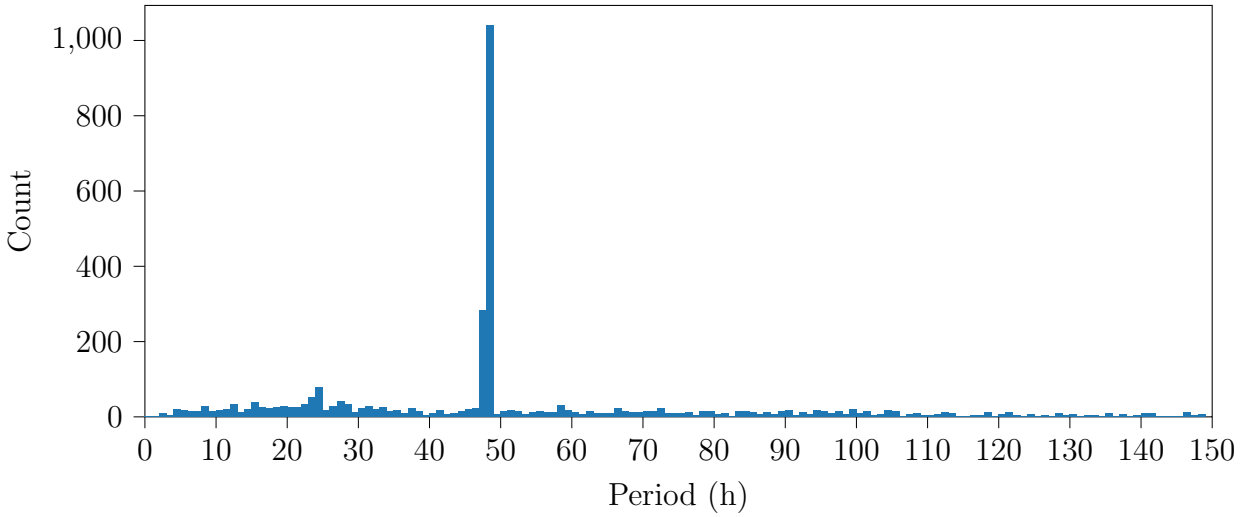

(c) Year 3

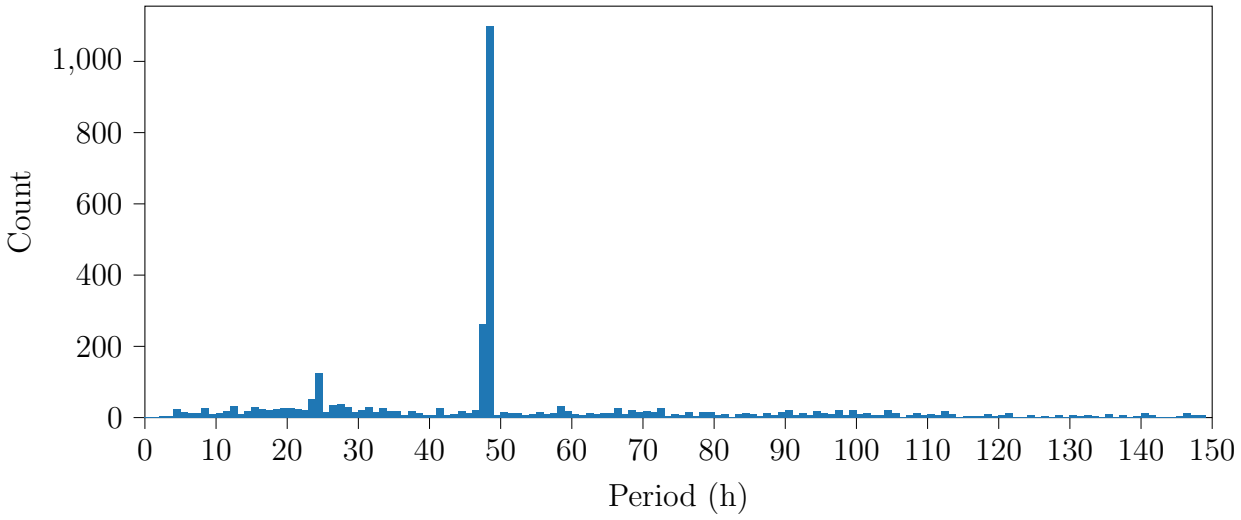

(d) Year 4

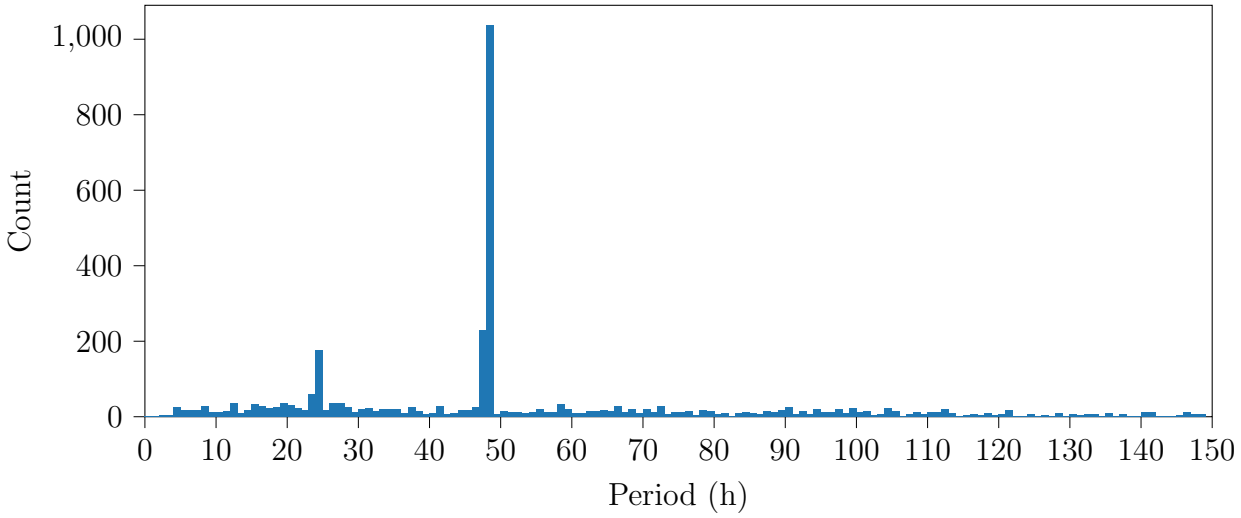

(e) Year 5

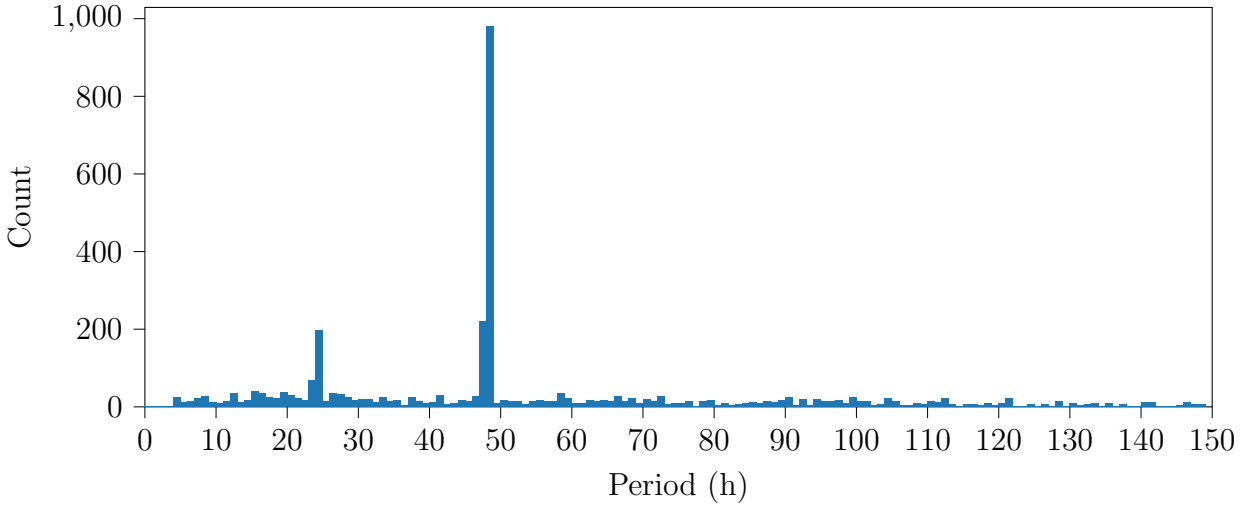

(f) Year 6

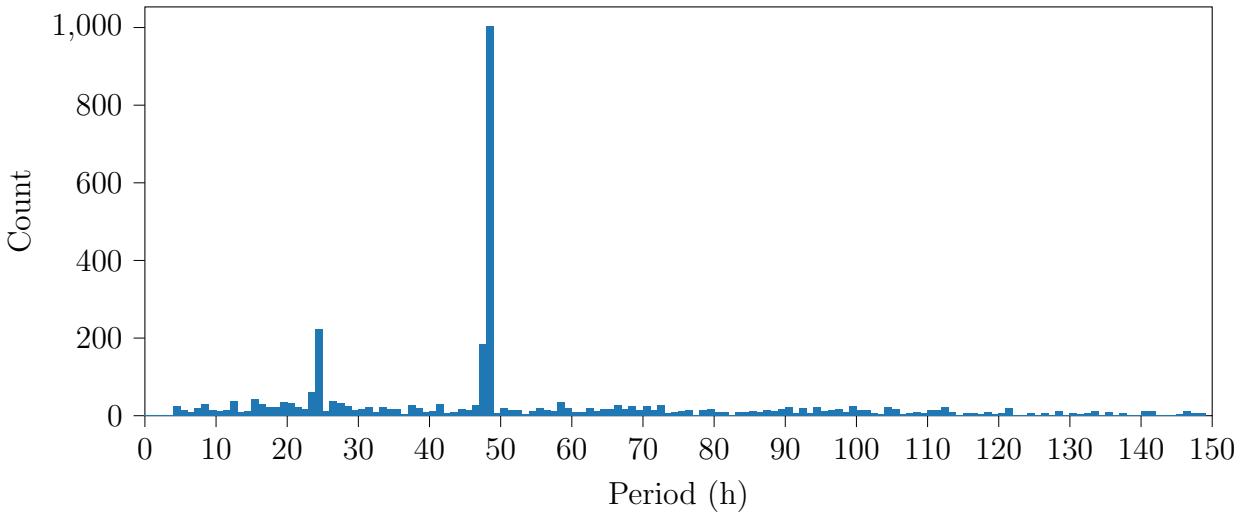

(g) Year 7

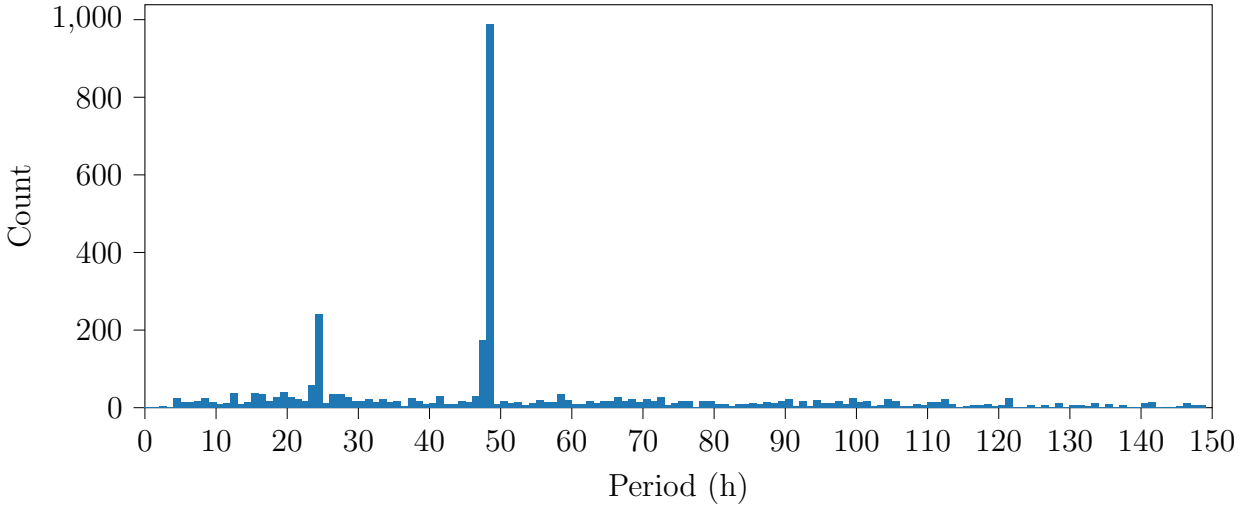

(h) Year 8

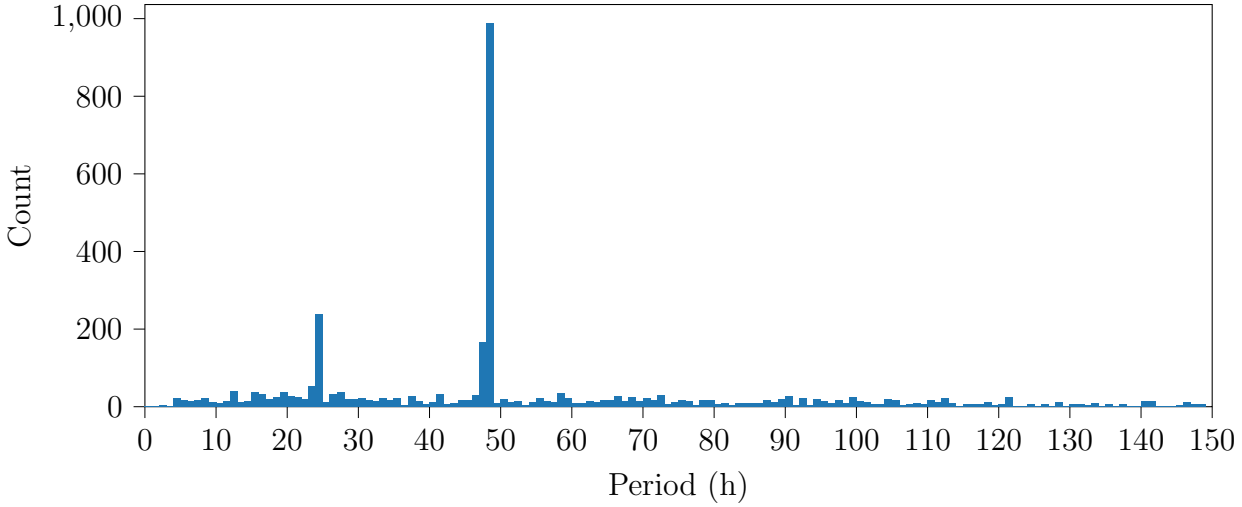

(i) Year 9

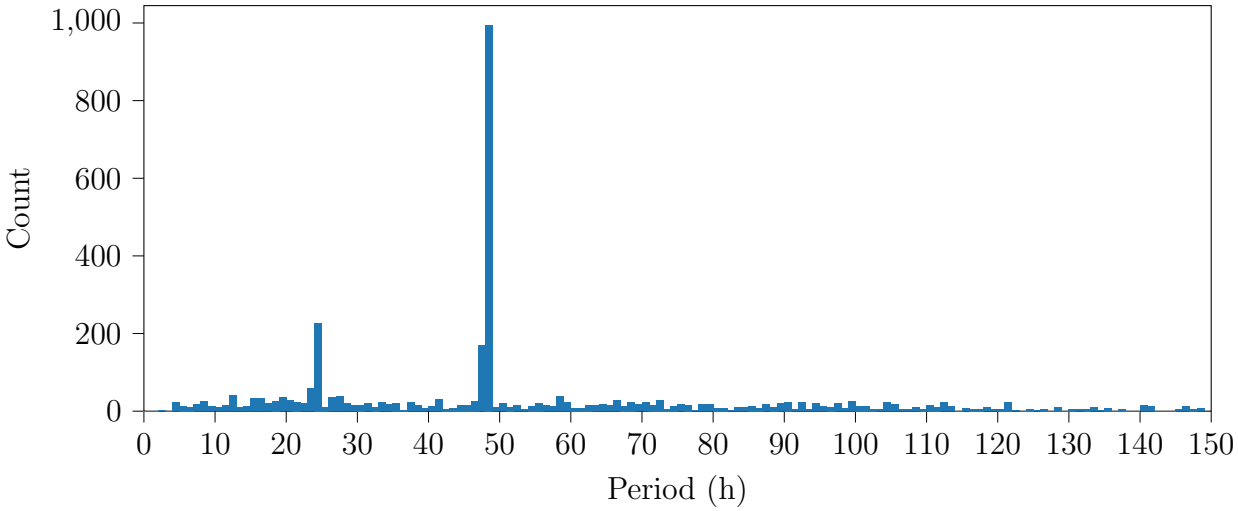

(j) Year 10

Figure A.7: The derived period distribution for each year of LSST.

Appendix B

On Deriving Periods

Deriving rotation periods can be a simple, but tricky process. In this thesis, periods have been derived several times, but here I will go into detail about how to get a period from raw, telescope data. This process will be for L-S; other period finding algorithms might need something slightly different.

1. Get the apparent magnitudes, times of observations, and filters. I recommend at least 50 observations for sparse data, but more or less can be used depending on the spacing, quality, and period of the data.

2. Obtain the distance from the Earth (or observer) to the object (Δ) in AU, the distance from the Sun to the object (r) in AU, and the Sun-object-Earth angle (phase angle, α) for each observation. A tool like JPL Horizons[1] can be used to obtain these values.

3. Calculate the light time correction (LTC), a value that is the time it takes the light reflecting off the object to the Earth, for each observation by the following equation $\text{LTC} = c\Delta$, where c is the speed of light. It is recommended to have the "time" unit of c be the same as your "time of observations" unit (usually days) and the "distance" unit be in AU. This results in $c \approx 173.1\,\text{AU/d}$

4. Subtract LTC from the time of observations. This value we will call t.

[1] `https://ssd.jpl.nasa.gov/horizons/app.html`

- If the observations are stored in a database, LTC, along with Δ, r, α, can be stored alongside each observation

5. Calculate the absolute magnitude of each observation. Information on how to do this can be found in Section C. We will call this value H.

6. Group the data by the filters the observations were taken in.

7. Calculate the mean of the absolute magnitudes, μ_H, in each group. Calculate a new value $H_0 = H - \mu_H$ for each group.

8. Combine the groups back together. The order of the observations does not matter for L-S.

9. Determine the period range you want to search and divide each by 2 (i.e. a period range of $[2\,\text{h}, 100\,\text{h}]$ would become $[1\,\text{h}, 50\,\text{h}]$). We are converting the *rotation* period to *light-curve* period. The lower-bound period will be called $p_{\min}$ and the upper-bound period will be called $p_{\max}$.

10. Determine a number of periods to check. Different sources suggest differing number of periods [24], but I suggest choosing a large value, like 5×10^6. We will call this value m. If time/memory are a concern, change the value to fit within your parameters, but remember that a fewer number of periods reduces your accuracy.

11. Construct an angular frequency grid ω_{grid} by creating an array of size m with evenly spaced values on $\left[\dfrac{2\pi}{p_{\max}}, \dfrac{2\pi}{p_{\min}}\right]$. It would also be useful to construct a period grid $p_{\text{grid}} = \dfrac{2\pi}{\omega_{\text{grid}}}$.

    - This step might change depending on what library you use to implement L-S as some will do this for you; I am assuming you are using SciPy's implementation [66].

12. Run your implementation of L-S using H_0, t, and ω_{grid}. Store the resulting periodogram into a variable. We will call this P (do not confuse the periodogram P for the period p).

13. This is the step where you would implement any de-aliasing. We will be ignoring this step for this guide.

14. The object's *light-curve* period will be $p_{\text{grid}}[\texttt{argmax}(P)]$. To obtain the *rotation* period, multiply this value by 2.

Appendix C

Phase Curve Fitting

Phase Curves are a result of physical properties of an object including its size and surface composition. Phase Curves are an often overlooked part of small body rotations as it determines the conversion from apparent magnitude to absolute magnitude. Absolute magnitudes are needed because most of the variation in apparent magnitude would be caused of the varying geometry caused by the orbit of the object and Earth.

There are several systems for small body phase curves, HG [13], $HG1G2$ [48], $HG12$ [48], and revised $HG1G2$ [51]. HG is the most commonly used, so that is what I will be discussing.

$$V(\alpha) = V_{\text{obs}} - 5\log(r\Delta) \tag{C.1}$$

A Phase Curve is a plot of the Sun-object-Earth angle (phase angle, α) vs the objects reduced magnitude ($V(\alpha)$). Reduced magnitude, which is given by Equation C.1 [13], where r is the Sun-object distance in AU and Δ is the Earth-object distance in AU, is a partially

geometry corrected magnitude. To fully correct it, Equation C.2 [13] is used:

$$\begin{aligned} 10^{-0.4V(\alpha)} &= a_1\phi_1 + a_2\phi_2 \\ H &= -2.5\log(a_1 + a_2) \\ G &= \frac{a_1}{a_1 + a_2} \end{aligned} \tag{C.2}$$

Where a_1 and a_2 are constants to solve for, ϕ_1 and ϕ_2 are given by Equation C.3 or C.4[1], H is the absolute magnitude, and G is the slope parameter. H and G will be gone over in more detail later in the section. Now, it is trivial show that the solving for H gives you Equation C.5.

$$\begin{aligned} \phi_i &= W\phi_{iS} + (1 + W)\phi_{iL} \\ W &= \exp\left(-90.56\tan^2\left[\frac{\alpha}{2}\right]\right) \\ \phi_{iS} &= 1 - \frac{C_i\sin(\alpha)}{0.119 + 1.341\sin(\alpha) - 0.754\sin^2(\alpha)} \\ \phi_{iL} &= \exp\left[-A_i\left(\tan\left[\frac{\alpha}{2}\right]\right)^{B_i}\right] \\ A_1 &= 3.332 \quad A_2 = 1.862 \\ B_1 &= 0.631 \quad B_2 = 1.218 \\ C_1 &= 0.986 \quad C_2 = 0.238 \end{aligned} \tag{C.3}$$

$$\begin{aligned} \phi_i &= \exp\left[-A_i\left(\tan\left[\frac{\alpha}{2}\right]\right)^{B_i}\right] \\ A_1 &= 3.33 \quad A_2 = 1.87 \\ B_1 &= 0.63 \quad B_2 = 1.22 \end{aligned} \tag{C.4}$$

[1]Equation C.4 is known as "simple" form

$$H = V_{\text{obs}} - [5 \log 10(r\Delta) - 2.5 \log 10([1 - G]\phi_1 + G\phi_2)] \tag{C.5}$$

It should be noted that the version of Equation C.5 in Bowell et al. [13] is incorrect. Bowell et al. [13] has $H(\alpha)$ labeled as apparent magnitude when it should be reduced magnitude.

H is related to the size of the object, where the smaller the H value, the larger the object. G determines the shape of the phase curve and it is related to the surface properties of the object, although the exact relation is not known. Bowell et al. [13] states that c-type small bodies have a mean G value of 0.15 and s-types have a mean of 0.25, but it is common for $G = 0.15$ for every object.

To solve for G, there is not a "nice" formula to use. The best way I have found is to fit H and G values to the object's phase curve. Since H and G values are mostly constrained (small bodies we can detect usually fall on the ranges of $3 \lessapprox H \lessapprox 30$ and $0 \lessapprox G \lessapprox 1$), using a bounded minimization method works best. Using bounds $\pm 10\%$ of the minimum/maximum values from Vereš et al. [65] should encompass most objects and the Powell minimization method [52] results in most objects having their H and G values found. A bonus to the Powell method is that it does not need the derivative of the function, which is not trivial to calculate.

I have made a python library that will do most of the phase curve work for you. It is available here[2].

[2] `https://pypi.org/project/phase-curve-tools/`